Title :

Oscillation-driven memory encoding, maintenance and recall in an entorhinal-hippocampal circuit model

Authors

Tomoki Kurikawa[1], Kenji Mizuseki[2], and Tomoki Fukai[3,4]

1. Department of Physics, Kansai Medical University, Hirakata, Osaka 573-1191, Japan
2. Department of Physiology, Osaka City University Graduate School of Medicine, Abeno-ku, Osaka, 545-8585, JAPAN
3. Okinawa Institute of Science and Technology, Onna-son, Okinawa 904-0495, Japan
4. RIKEN Center for Brain Science, Wako, Saitama 351-0198, Japan

Abstract

Coherent neuronal activity phase-locked to theta and gamma oscillations is thought to be crucial for information processing across multiple brain regions. However, the network mechanisms underlying the oscillation-driven multi-area computation remains largely unclear. To explore such mechanisms, we constructed a hippocampal-entorhinal neural network model involving parvalbumin-positive, somatostatin-positive and vasoactive intestinal polypeptide interneurons in the hippocampal area CA1 and the superficial and deep layers of the entorhinal cortex. We examined the model behavior by using neural activity data recorded during delayed nonmatching to place tasks. Our model shows that experimentally observed relative phases of theta oscillation ensure working memory performance. Moreover, the model predicts that acetylcoline concentrations in these areas modulate the balance between intra-area and inter-area information processing according to cognitive demands emergent at encoding, maintenance and recall epochs of a working memory task. Our model suggests the active role of theta-phase-locked firing and cholinergic modulations for multi-area memory processing.

Acknowledgement

We thank Jun Yamamoto for providing experimental data and fruitful discussion and György Buzsáki for publicly sharing the valuable data. This work was supported by KAKENHI (nos. 18H05213 and 19H04994) from the MEXT.

Spatial navigation is a fundamental cognitive function that requires the processing of spatial memory by the hippocampus and entorhinal cortex. During a spatial navigation task, spatial information relevant to the task has to be encoded into, maintained in and recalled from spatial working memory at adequate times. How these operations are coordinated by the cortico-hippocampal neural circuits during a spatial working memory task has to be yet explored.

A spatial working memory task is processed by several cortical areas such as the medial prefrontal cortex (mPFC) (Benchenane et al., 2010; Jones and Wilson, 2005; Spellman et al., 2015), medial entorhinal cortex (MEC)(Suh et al., 2011; Yamamoto et al., 2014) and the hippocampal area CA1 (Benchenane et al., 2010). These anatomically connected areas (Eichenbaum, 2017; Swanson and Cowan, 1977; Witter et al., 2000) are thought to mutually communicate information necessary to accomplish the task. Interestingly, the degree of functional importance of different inter-area connections varies during the task. This is suggested because the impairment of these connections at different behavioral phases differentially influenced task performance (Spellman et al., 2015; Suh et al., 2011; Yamamoto et al., 2014). For instance, in a delayed nonmatching to place task (DNMP), the maintenance of spatial memory during a delay period does not require synaptic connections from the layer 3 of the MEC (MECIII) to CA1, but these connections are necessary for memory recall(Yamamoto et al., 2014). Connections from CA1 to the mPFC play a crucial role in memory encoding but not in memory recall (Spellman et al., 2015). These results indicate that information flows via the hippocampal circuit are not static but are dynamically regulated depending on the behavioral demands.

Coherence in neuronal activity between different areas likely reflects dynamic information routing across multiple areas (Spellman et al., 2015; Yamamoto et al., 2014), which leads to the hypothesis called “communication through coherence”(Fries, 2015). Many theoretical (Akam and Kullmann, 2010; Buehlmann and Deco, 2010; Palmigiano et al., 2017; Vogels and Abbott, 2005; Yang et al., 2016) and experimental

(Letzkus et al., 2015; Womelsdorf et al., 2014) studies have explored the gating functions for this dynamic processing. However, how the computations installed at multiple cortical areas are integrated to execute a spatial working memory task remains largely unclear. In addition, the mechanistic role of theta and gamma oscillations in this process has not been fully understood.

Here, we elucidated the underlying mechanisms of multi-area dynamic information processing during spatial navigation. In so doing, we constructed a biologically plausible model of the entorhinal-hippocampal circuit consisting of MECIII, CA1 and MEC layer V (MECV). We show that the model successfully reproduces a wide range of behavioral and electrophysiological observations reported from a DNMP task (Yamamoto et al., 2014). We further confirmed the validity of the model by using data from another DNMP task (Fernández-Ruiz et al., 2017; Mizuseki et al., 2013). Importantly, our model predicted the crucial role of cholinergic modulations in regulating information flow dynamics of the MECIII-CA1-MECV circuit. Acetylcholine (ACh) is related to cognitive states (Hasselmo and Sarter, 2010; Parikh et al., 2007) in many behavioral tasks including fear conditioning (Letzkus et al., 2011; Pi et al., 2013), sensory discrimination (Hangya et al., 2015; Pinto et al., 2013), associative memory (Sabec et al., 2018), and spatial (Croxson et al., 2011; Okada et al., 2015) and non-spatial working memory tasks (Furey et al., 2000; Hasselmo, 2006; McGaughy et al., 2005). Consistent with the regulatory role, cholinergic inputs from the medium septum (MS) project broadly to distinct cortical areas including the hippocampus. In our model, cholinergic modulations were necessary to perform the three important stages of memory processing, i.e., encoding, storing, and decoding spatial information and were implemented by disinhibitory mechanisms.

Results

Hippocampus-entorhinal cortex circuit model

To understand the circuit mechanisms to control flexibly spatial information in the hippocampus and MEC, we built an inter-areal cortical network model (Figure 1A, see

Supplemental materials for details). The network comprises three main areas CA1, MEC layer 3 (MECIII) and layer 5 (MECV), and additional areas CA3, MEC layer 2 (MECII) and medial septum (MS) as external inputs. All main areas have excitatory (E) and parvalbumin (PV)-positive interneurons. In addition to these neurons, the model CA1 has somatostatin (SOM)-positive oriens-lacunosum moleculare (OLM) and vasoactive intestinal polypeptide (VIP) neurons. We built synaptic connections in our model based on anatomical observations (Gonzalez-Sulser et al., 2014; Unal et al., 2015; Witter et al., 2000). In addition, we assumed that E neurons in MECII project to PV neurons in MECIII, as previously suggested (Mizuseki et al., 2009).

Exc, PV and OLM neurons constitute the core circuits of the present network model and were modeled as Hodgkin-Huxley-type conductance-based neurons according to previous models (Middleton et al., 2008; Rotstein et al., 2006; Wang and Buzsáki, 1996; Wulff et al., 2009). VIP neurons were modeled as Poisson firing neurons with the probability density of spikes described and their outputs mediate the modulatory effect of acetylcoline (ACh). We described CA3 excitatory neurons projecting to CA1, MECII E neurons projecting to MECIII, and GABAergic neurons in MS projecting to CA1 and MECV as external Poisson spike trains. As shown in Figure 1B, the firing probabilities of these neurons were modulated at the theta frequency (10Hz) to induce theta rhythmic activities in the core circuits. The relative preferred phases of the theta rhythm of the external inputs were adjusted based on experimental observations (Klausberger and Somogyi, 2008; Mizuseki et al., 2009). Furthermore, from these phases and experimental observations, we set the theta phase of the local field potential (LFP) to be observed in the stratum pyramidale (SP) of CA1. Although this LFP was not directly calculated from the modeled CA1 activities, the quantity was used as a reference to measure the degree of agreement between the preferred phases of model neurons and experimental observations. The preferred phases of GABAergic neurons in MS were dependent on their target neuron types (ECV PV, CA1 PV and CA1 OLM). In experiment, GABAergic neurons projecting to OLM and those projecting to PV in CA1 have different preferred phases (Borhegyi, 2004).

Acetylcholine is known to modulate activity of VIP neurons (Albuquerque et al., 2009) and the conductance of a calcium-sensitive non- specific cation current (CAN) in MECV excitatory cells (Fransen et al., 2002; Fransén et al., 2006) in a manner depending on the concentration of ACh ([ACh]). In this study, we test the hypothesis that [ACh] varies in correlation with cognitive demands to perform encoding, maintenance and decoding spatial working memory. We demonstrate that the cholinergic modulations of disinhibition of CA1 E neurons and calcium dynamics in MECV E neurons enable the flexible processing of spatial working memory. Cholinergic neurons in MS ((Newman et al., 2012; Zhang et al., 2010) were not explicitly modeled.

For Poisson neurons in CA3, MECII and MS, their preferred phases of theta oscillation for the default [ACh] (Figure 1D) were chosen to be consistent with experimental observations (Borhegyi, 2004; Klausberger and Somogyi, 2008; Mizuseki et al., 2009). Given this condition, all neurons in CA1, MECIII and MECV fired in theta-rhythmic manners (Figure S1A). As observed in experiments, E and OLM neurons in CA1 showed preferred phases around the troughs of theta oscillation, whereas PV neurons around the peaks (Klausberger and Somogyi, 2008). In MECIII, E and PV neurons fired preferentially around the peaks and troughs of theta oscillation, respectively (Mizuseki et al., 2009). In MECV, PV neurons preferred the troughs, but E neurons did not show strong phase preferences (Mizuseki et al., 2009). These results show that theta phase-locked firing in our model is biologically plausible.

Encoding spatial information into theta rhythmic firing

The central question of this study is to clarify how spatial information is encoded, maintained and recalled in the entorhinal-hippocampal circuits. To study this problem, we asked whether our model can replicate the task-related activities reported in previous experiments. In particular, we considered a DNMP task on a T-maze (Yamamoto et al., 2014). In this experiment, one arm of the T-maze was closed during a sample run and the rat was forced to choose another arm. After a delay period, the

rat was set to a test run in which both arms were open and the rat had to choose the arm opposite to the one chosen in the preceding sample run (that is, if the rat chose the right arm in the sample run, it had to choose the left arm in the test run). For a successful test run, the rat had to remember the previously chosen arm. This task requires at least two types of memory, namely, rule-based memory and spatial working memory. The former memory is thought to be encoded in the prefrontal cortex (Durstewitz et al., 2010; Guise and Shapiro, 2017; Preston and Eichenbaum, 2013). However, in this study we did not model the prefrontal circuits and focused on the processing of spatial working memory in the entorhinal-hippocampal circuits.

Figure 1C shows the organization of sample and test runs in our model together with the connectivity patterns between the neural ensembles encoding different locations on the maze. We monitored the activity of sample runs along the center arm (sample-C) and left arm (sample-L), and that of test runs at the home position (delay) and center arm (test-C) up to the junction (decision point) of the T-maze. For the sake of simplicity, we implemented four subgroups L, R, C and H of place cells in CA3, each of which represented the current position of the model rat on the left, right, center arms and at the home position, respectively. For instance, neurons belonging to the subgroup L were given a higher firing probability when the model rat traveled across the left arm (Figure 1D; also see "Neuron models" in STAR methods). Accordingly, E neurons in CA1 were also divided into four subgroups L, R, C, and H, each of which was strongly projected to by the corresponding subgroup in CA3. In contrast, MECIII and MECV had two subgroups denoted as L and R, and these subgroups were assumed to form closed loop circuits with the corresponding CA1 subgroups. The other positions on the maze that are not shown in Figure 1C were not modeled.

Role of theta oscillation in coordinating activities in the CA1-MECV-MECIII loop circuit

Experimental results showed that theta-phase-locked firing in MECIII is highly correlated with the task performance (Yamamoto et al., 2014). Therefore, we hypothesized that the L and R subgroups in MECIII contributes to the success of spatial

working memory task and defined task performance as difference in neural activity between these subgroups at the test-C period. The larger the difference is, the more robust the memory encoding is. Below, we consider the case, without loss of generality, that the rat chooses the left arm in every sample trial. In Figure 1D, we demonstrated activities of E neurons in CA3, CA1, MECV and MECIII together with [ACh] during (1) sample-C, (2) sample-L, (3) home (delay) and (4) test-C runs. Depending on the rat's position, the corresponding subgroup was activated in CA3. During the sample-L run, [ACh] was increased, which disinhibited CA1 PV neurons and accordingly strongly activated the CA1-MECV-MECIII loop circuit of the L subgroups to encode a choice memory in MECIII. Then, in the delay period, [ACh] was slightly decreased, which strongly suppressed neural activities in all L subgroups including the CA1 subgroup L. We note that a similar suppression arose in experiment as if spatial memory had not been maintained during delay periods (Yamamoto et al., 2014). During the test-C run, the CA1 subgroup C was activated driven by the CA3 subgroup C. Importantly, as the model rat approached to the decision point, the subgroups L were gradually reactivated in the loop circuit to retrieve the memory of the previous choice. This activation-suppression-reactivation pattern is clearly seen in the firing rate of MECIII neurons. Average firing rates during the test-C period were significantly different ($p=3.071\times10^{-6}$, *t* test on two related samples) between the subgroups L and R in MECIII (Figure 1E), implying that the network model successfully recalled the stored spatial memory.

The successful encoding of memory required theta-phase-locking of neural firing along the CA1-MECV-MECIII loop circuit. As mentioned previously, the theta phases of external sources (i.e., CA3, MECII and MS) entrain neurons in these areas in theta-phase-locked firing with the preferred phases that are consistent with experimental observations. In the normal situation, MECIII PV neurons are activated by input from MECII at the bottoms of theta oscillation and consequently MECIII E neurons tend to fire at the peaks. Then, CA1 E neurons are strongly activated in non-linear manner(Bittner et al., 2015; Takahashi and Magee, 2009) by near-coincident inputs

from MECIII and CA3: spikes from CA3 arrive at CA1 at the descending phases of theta oscillation just after spikes from MECIII (see STAR Methods).

The theta phases of inputs from different sources need to be well coordinated for successful working memory function. To examine this, we shifted the preferred phases of MECII neurons by 180 degrees from the troughs to the peaks of the reference theta oscillation of CA1 LFP (Figure S1B). Figure S1C shows the phase preferences of CA3, CA1 E, CA1 PV, and MECIII E neurons after this change. MECIII PV neurons dramatically reduced spikes at the descending phases of theta oscillation, which shifted the firing of MECIII E neurons to the troughs of theta oscillation. Consequently, the peak activities of MECIII and CA3 were separated by about one half of theta cycle and did not coincidently innervate CA1. The timing deviation impaired the encoding of spatial information into the loop circuit, as indicated by significantly reduced rate differences between L and R subgroups (Figure S1D, $p= 2.679 \times 10^{-16}$, *t* test on two related samples), resulting in a degraded task performance (Figure 1F, $p= 2.334 \times 10^{-8}$, *t* test on two related samples). Thus, theta oscillation is crucial for the appropriate temporal coordination of neuronal firing in the entorhinal-hippocampal circuit.

Figure 1. Entorhinal-hippocampal network model. (A) The structure of the network model is schematically illustrated. (B) Theta-modulated firing probabilities of input neurons are shown during the sample-center run. The preferred firing phases were determined with respect to a reference theta oscillation (black) reported in the CA1 stratum pyramidale (SP) layer. (C) Left; Schematic illustrations of task periods during the sample and test trials of the DNMP T-maze task: (1) sample-C, (2) sample-L, (3) home (delay), (4) test-C periods. Right; Synaptic connectivity is shown between the neuron subgroups encoding the specific locations of the maze (left, right, center arms and home position). Connections (bold) are stronger within the loop circuit of MECV, MECIII and CA1 than other modest connections (solid). (D) Raster plots of E neurons in different cortical areas are shown together with the time evolution of ACh concentration. (E) The average firing rates of MECIII L and R subgroups were calculated

for the test-C period in five different networks with five different initial conditions (black lines). Unless otherwise stated, average firing rates were evaluated in a similar fashion throughout this study. (F) Probability of left choice (P_L) and average of P_L was calculated in the normal and modified conditions. Gray dots show P_L of different networks for different initial conditions. Here, $P_L = e^{-r_L}/(e^{-r_L} + e^{-r_R})$, where r_L, r_R are firing rate of L and R subgroups in test-C period, respectively. Chance level is 0.5.

Figure S1 (related to Figure 1). Activity of various types of neuron during task. (A) Preferred phases of various neuron types during the sample-C period. The firing rates were calculated by numerical simulations for excitatory and inhibitory neurons in the entorhinal-hippocampal circuit. The reference theta oscillation presumed in the SP layer of CA1 is also shown (solid lines). (B) Theta-modulated firing probabilities of ECII neurons for the normal and preferred phase shift conditions are shown. (C) Modulations of spike counts by theta oscillation are shown for CA1 E, MECIII E and MECIII PV neurons during the sample-L period. Neuronal activities in the normal and preferred phase shift conditions of theta oscillation are shown with dark and light colors, respectively. (D) Differences in the firing rate between the L and R subgroups of CA1 E neurons were calculated during the sample-L period and compared between the normal and the phase shift conditions. Simulation results for the same initial conditions are connected with lines.

The role of disinhibition in regulating the activity of the CA1-MECV-MECIII loop circuit

We show that the ACh-mediated disinhibitory mechanisms regulate cross-area communications within the entorhinal-hippocampal circuit during different task periods. We first analyzed how CA1 neurons selectively encode spatial information from CA3. We consider the default state (i.e., 0 to 1 sec in Figure 1D) in which [ACh] is low (Figure 2A). In this state, output from VIP neurons is weakened and, consequently, PV neurons are strongly activated around the peaks of theta oscillation (Figure 2B). Accordingly, CA1 E neurons rarely fire around the peaks (but they can generate a small number of spikes driven by external noise after the troughs of theta oscillation at

which inputs from both PV and OLM are weakened: see Figure S1A). In contrast, during the epochs of high [ACh] (Figure 2D, the sample-L period: the test-C period also corresponds to the high [ACh] epoch, but will be discussed later), CA1 E neurons show strong activation immediately after the peaks of theta oscillation because PV neurons are suppressed around the peak (Figure 2E). OLM neurons are also suppressed, but their inhibitory effect on E-neuron firing around the peak is relatively weak since the preferred phase of OLM neurons is the trough of theta. Thus, the cholinergic modulation advances the preferred phase of CA1 E neurons from the troughs to the peaks of theta oscillation. Later, we will examine the model's prediction in experimental data.

Information on the current position of the rat can be transferred from CA3 to CA1 only when [ACh] is sufficiently high. Throughout the task, CA1 E neurons constantly receive position information from CA3 which changes as the rat moves on the maze. During encoding epoch, a certain mechanism is required to enable CA3 inputs to activate CA1 neurons in the sample-L period (see the CA1 L subgroups in Figure 1D). ACh-induced disinhibition provides this mechanism: at the sample-C period [ACh] is low and the sensitivity of CA1 E neurons to CA3 input remains low, consequently the position information is not transferred to CA1; at the sample-L period [ACh] is increased and accordingly the sensitivity is also enhanced, resulting in an information transfer (Figures 2C and 2F).

The disinhibition mechanism further explains why the blockade of MECIII-to-CA1 connections impaired task performance in experiment (Yamamoto et al., 2014). When the model rat is sampling left or right arm, the disinhibition mechanism enables the activation of the corresponding subgroups in the CA1-ECV-ECIII loop: highly activated CA1 neurons activate MECV E neurons, which in turn activate MECIII E neurons. MECIII-to-CA1 projections further activate CA1 E neurons, thus completing a positive feedback loop within the activated subgroups. However, the blockade of MECIII-to-CA1 connections reduces neural activity in CA1 and hence in MECIII, disabling the storage of

the current position.

To confirm the crucial roles of disinhibition (i.e., VIP-PV-E and VIP-OLM-E connections) in the working memory task, we studied two cases. In the first case, PV neurons were inactivated in CA1 during the entire trial period without changing the other conditions (Figure S2A). Due to the lack of inhibition from PV neurons, CA1 E neurons were strongly activated at any ACh concentration. In the encoding epoch, E neurons exhibited higher activity in the L subgroup than in the R subgroup in both CA1 (Figure S2B) and ECIII (Figure S2C, 1 to 3 sec). However, after this epoch E neurons immediately lost selectivity to spatial information because they were too strongly activated in both subgroups. During some intervals firing rate was higher in the L subgroup than in the R subgroup, but it was opposite during other intervals (Figure S2C, after 3 sec). Thus, the spatial information recalled randomly varied from trial to trial, and working memory performance was unreliable (Figure S2D).

In the second case, the cholinergic modulation of PV neurons (but not that of OLM neurons) was terminated during the entire trial period. In this case, PV neurons were not inactivated even at high [ACh] (Figure S2E) and the encoding of spatial information into CA1 was largely impaired (Figure S2F). Consequently, spatial information could not be stably maintained in MECIII (Figure S2G) and probability of left choice, P_L, was significantly decreased (Figure S2H, $p=1.542\times10^{-9}$, *t* test on two related samples). Thus, in both cases, spatial information in CA3 was not successfully transferred into the CA1-MECV-MECIII loop circuit.

Figure 2. Gating of CA3-to-CA1 signaling by disinhibition mechanism. (A) The operation mode of disinhibitory circuit is schematically illustrated in low [ACh] states. (B) Theta phase preferences of spiking during the sample-C period are shown for CA1 neurons. Only for VIP neurons, the firing rate normalized by [ACh], which corresponds to output from VIP neurons to other inhibitory neurons (see the STAR method), is plotted. Solid curves show the reference theta oscillation. (C) Average firing rates of

the L, R, C and H subgroups in CA3 and CA1 are shown during the sample-C period. (D) The operation mode of disinhibitory circuit in high [ACh] states. (E, F) Similar to (B) and (C) during the sample-L period.

Figure S2 (related to Figure 2). Effect of inactivation of disinhibition mechanism. (A) Firing rates of CA1, CA3 and MECIII neurons during sample-L periods are shown. During the simulations, CA1 PV neurons were inactivated. Solid curves indicate the reference theta oscillation. (B) Average firing rates of CA1 E neurons in different subgroups are plotted during sample-L periods in the same inactivating condition. (C) Raster plots are shown for the L (blue) and R (orange) subgroups of MECIII E neurons. (D) Probability of left choice is plotted in the normal and inactivating conditions. Lines connect two data points obtained from simulations of a normal network and its impaired version with the same initial conditions. (E, F, G, H) same as (A) to (D), but for the network models with disabled VIP-to-CA1 PV connections.

Covert activation by calcium dynamics

An unexpected experimental finding was that neural activities in MECIII were strongly suppressed during delay periods (Yamamoto et al., 2014). This observation challenges our hypothesis that either MECV or MECIII, or both, serve for working memory in the spatial decision making task, raising the question about how the entorhinal-hippocampal circuit recalls the encoded spatial information after the delay periods. To explore the underlying circuit mechanisms of memory recall, we implemented calcium-sensitive non-specific cation current (CAN current in STAR Methods) in our cortical neuron models.

The CAN current was originally proposed to explain persistent activity of single cortical neurons in MECV (Fransen et al., 2002; Fransén et al., 2006), and a similar persistent activity was later shown in the layer V of various cortical areas (Rahman and Berger, 2011). The CAN current is activated in the presence of ACh with the intensity depending on the activation rate of high conductance channels, r_H. The conductance r_H

is linearly increased when the calcium concentration [Ca^{2+}] is beyond a critical value d_P and decreased when [Ca^{2+}] is below another critical value d_D. Because $d_D < d_P$, a hysteresis effect or bistability appears for $d_D <$ [Ca^{2+}] $< d_P$. Thus, once [Ca^{2+}] exceeds d_P, the value of r_H remains high until [Ca^{2+}] again decreases below d_D (Figure 3A). Neurons with high r_H respond to input more sensitively than those with low r_H and, thus, memory of previous high activity is stored in r_H through calcium dynamics.

In the sample-L period, an increased activity of the CA1 subgroup L enhanced spike firing of MECV E neurons in the subgroup L (Figure 3B). During the enhanced firing, [Ca^{2+}] was elevated in these neurons by calcium influx through the voltage-dependent calcium channel. This increase of [Ca^{2+}] occurred only in the MECV subgroup L but not in the MECV subgroup R (Figure 3C). After the sample-L period, [ACh] was decreased and, consequently, the CAN current was also decreased. Because lowering [ACh] decreased the output of VIP neurons, that of PV neurons was increased and consequently that of CA1 E neurons was suppressed. Thus, the changes in neural activity resulted in a decreased firing rate of MECV E neurons. Nevertheless, the fraction of high conductance state remained high in the subgroup L (but not in the subgroup R) of MECV E neurons (Figure 3C).

The CAN current plays a crucial role in the maintenance of working memory. To explain this, we divided the test-C period into early and late periods: in the early period CA1 neurons were selectively activated in the subgroup C but not in the subgroup L (and subgroup R); in the late period they were strongly activated in the subgroup L (Figure 3B). During the test-C period, [ACh] was again increased, so was the activity of CA1 E neurons through the disinhibition mechanism. Although MECV neurons in both subgroups L and R received synaptic input from the CA1 subgroup C, MECV neurons were selectively activated in the subgroup L because the high conductance rate remained high in these neurons. The activity of the MECV subgroup L neurons gradually increased in the early test-C period, and eventually became sufficiently strong to activate MECIII subgroup L neurons. Accordingly, the test-C period entered

the late period and the spatial information stored in MECV could be decoded by CA1 neurons. The onset time of the late period depends on the realization of neural networks and initial conditions. Thus, the covert activation of CAN current enables the retrieval of persistent activity in the MECV subgroup L neurons for the decoding of spatial information in the test-C period.

Figure 3. Role of CAN current in memory encoding and maintenance. (A) Single trial evolution of the membrane potential (top), [Ca^{2+}] (middle) and the ratio of high conductance state of CAN current (bottom) are plotted in an MECV excitatory neuron. Dots above the membrane potential represent spikes. Broken lines denote two threshold values, d_P and d_D, in the middle panel and the upper and lower critical values of the high conductance ratio in the bottom panel (See STAR method). (B) Firing rates are shown for E neurons in CA1, MECIII and MECV. Colors indicate different neuron subgroups. (C) Time evolution of [Ca^{2+}] (top) and the high conductance ratio (bottom) are plotted for randomly-chosen five MECV E neurons belonging to L (blue) or R (orange) subgroup during the same trial as in B.

Comparison of MECIII neural activity between the model and experiment

We compared the responses of our model with those of the rat entorhinal-hippocampal circuit. For this comparison, we analyzed E neuron activity in MECIII after dividing each of the sample-L, delay and test-C periods into early and late portions, respectively. As in experiment (Yamamoto et al., 2014), we first quantified the intensity of theta oscillation in these task periods by computing periodicity index. As shown in Figure 4A, this index was high during the late sample-L, early delay, and late test-C periods, but it was low during delay period (i.e., late delay and early test-C periods). Periodicity index exhibited similar task period-dependence in the model and experiment (c.f. Figure 5C and Figure S5 in (Yamamoto et al., 2014)).

We next analyzed how the blockade of MECIII-to-CA1 projection affects the behavior of

our model in different task periods. In the experiment, this blockade significantly impaired working memory performance of the rat. When MECIII-to-CA1 projection was blocked during the encoding epoch (sample-L period), MECIII activity and the firing rate difference between L and R subgroups were suppressed during both sample-L and the subsequent late test-C periods (Figure 4B, blue), meaning that task performance was impaired. When the blockade was during the recall epoch (late test-C, 5.5-7.5 s), the inter-subgroup difference was reduced and task performance was also impaired (green line in Figure 4B). In contrast, when the blockade was imposed during sample-C (3-4.5 s) or early test-C period (4.5-6 s), MECIII activity was not greatly affected (Figure S3). Figure 4C summarizes the resultant task performance of the model. In three of the four conditions (blockade in sample-C, early and late test-C), results were well consistent with experimental observations (c.f., Figure 6F in (Yamamoto et al., 2014)). In addition, our model predicts that the blockade in sample-L period significantly impairs working memory performance ($p=3.175\times10^{-10}$), suggesting that the CA1-MECV-MECIII loop circuit maintains neural activity in the MECIII and plays a pivotal role in the spatial working memory task. This prediction should be experimentally validated.

Figure 4. Blockade of MECIII-to-CA1 connections during sample-L and late test-C periods. (A) Periodicity index (Yamamoto et al., 2014) was calculated for the activity of MECIII E neurons (STAR methods). The labels L, D, C refer to sample-L, delay, test-C periods, respectively, and the numbers 1 and 2 label the early and late portions, respectively, of these periods. **(**B) Average differences in firing rate between the L and R subgroups of MECIII E neurons were calculated under the blockade of MECIII-to-CA1 connections: normal condition (black); the blockade during sample-L periods (blue); the blockade during late test-C periods (green). In each condition, the differences were averaged over five networks and five initial states. By definition, green and black lines overlap with one another before the blockade. Boxes above the traces indicate the periods of blockade. (C) P_L (same as in Figure 1F) were calculated for different periods of the blockade.

Figure S3 (related to Figure 4). Blockade of MECIII-to-CA1 connections during sample-C and test-C periods. Connections from MECIII to CA1 were blocked during sample-C (blue) and early test-C (green) periods. Differences in firing rate between the L and R subgroups of MECIII E neurons are shown in the same manner as in Figure 4B. Similar evolutions are also shown in the normal condition (black).

Experimental validation of period-dependent preferred theta phases

Our model predicts that CA1 E neurons shift their preferred theta phases from the troughs to the peaks when [ACh] is high (Figures 2B and 2E). In Figure 5A, we present the phase preference of CA1 E neurons during sample-C, sample-L, delay, early test-center (test-C1) and late test-center (test-C2) periods of the DNMP task. Their spikes preferred the troughs of theta oscillation during sample-C periods but, owing to the disinhibitory mechanism, the preferred phase was shifted to the peaks during sample-L periods (Figure 2B). When the model rat returned to the home position (delay period), [ACh] was decreased to reactivate PV neurons in CA1, which reduced the sensitivity of CA1 to inputs from MECIII and CA3 and selectively suppressed spike generation at the peaks of theta oscillation (but not at the troughs). In test-C1 periods, [ACh] was again increased to allow the activation of CAN current (Figure 3C), which shifted the preferred phase to the descending phase of theta oscillation. During test-C2 periods, our model predicts a progressive advance of preferred theta phase in CA1 due to an enhanced synaptic drive by MECIII (Figure 3B).

We confirmed these predictions in the data of a DNMP task in T-maze (Yamamoto et al., 2014). Figure 5B shows the distributions of preferred phases of spikes in rat CA1 during different task periods, i.e., sample-C, sample-L (corresponding to the reward arm), delay, test-C1, and test-C2 periods (see STAR Methods). In rats, spikes were generally not modulated by theta oscillation as strongly as in the model. In particular, oscillatory modulations were weak in sample-C periods. Nonetheless, the preferred theta phases in the various task periods are well consistent between rats and models.

The average preferred phase is delayed during delay periods compared to other task periods in both rats and models (Figure 5C). In addition, our model predicts that the preferred phase is progressively advanced during test-C2 (i.e., late test-center) period due to an increased synaptic drive by MECIII (Figure 3B).

Next, we asked whether preferred theta phase behaves similarly in an alternating figure-eight task (Mizuseki et al., 2013). We were particularly interested in examining the hypothesized role of cholinergic control of working memory function. In the alternating figure-eight task, rats were trained to alternately change the turn direction at a junction point of an eight-shape maze, meaning that the rats had to remember the turn direction of the preceding run. This task is similar to the previous DNMP task, but one difference is that sample and test trials are not clearly separated in the alternating figure-eight task. Nevertheless, we may correlate the behavioral epochs of the two tasks to each other. When rats traverse the center arm, they had to retrieve memory of the preceding choice to prepare for the next choice. Therefore, traveling along the center arm may correspond to test-C period in the DNMP task. Then, we can define three distinct areas on the eight-shape maze (Figure 5D): early center, late center and reward arms, which may correspond to test-C1, test-C2 and sample-L periods, respectively. Below, we follow these rules.

Figure 5E shows the preferred phases of excitatory neurons in the deep layer of CA1. It has been reported that for some unknown reason these neurons only exhibit phase shifts in early trials (Fernández-Ruiz et al., 2017; Mizuseki et al., 2013). Therefore, we only used data of initial ten trials in the following analyses. On the early center arm (test-C1 period), neurons fired more frequently around the troughs of theta oscillation than the peaks. However, on the late center arm (test-C2 period), neurons fired slightly more often at the peaks, generating two peaks per theta cycle in the spike density distribution. On the reward arm (sample-L period), neurons fired most frequently at the peaks, which is consistent with the previous study(Fernández-Ruiz et al., 2017). These results seem to be consistent with the model's prediction that the preferred

516 firing phase of CA1 neurons changes from the troughs to the peaks of theta oscillation
517 during the epochs of high [ACh]: in the alternating figure-eight task, high level of
518 attention, or high [ACh], is likely to be required on the reward arm (for encoding
519 reward information) and the late center arm (for recalling the previous choice).
520
521 **Figure 5. Preferred theta phases in model networks and rats.** (A) Phase preferences
522 are shown for CA1 E neurons in model networks during given task periods (top). (B)
523 Phase preference curves of CA1 neurons were calculated for data obtained in
524 (Yamamoto et al., 2014). (C) Preferred theta phases of the models (filled circles) and
525 rats (empty circles) were averaged over multiple theta cycles during given task periods.
526 The average phase $\bar{\theta}$ is computed as $\bar{\theta} = \arg\left(\Sigma_{\mathrm{k}} \exp(i\theta_k)\right)$, here, k is index of spikes
527 for all neurons and i is imaginary unit. The same average phases are shown for two
528 theta cycles (one in darker colors and one in light colors) for the clarity of the plots. (D)
529 Schematic illustration of the figure-eight maze used in (Fernández-Ruiz et al., 2017;
530 Mizuseki et al., 2013). Colored rectangles indicate early-center, late-center, and reward
531 periods from which data were resampled. (E) Phase preference curves of CA1
532 excitatory neurons were calculated by using the data of (Mizuseki et al., 2013). For
533 comparison, we divided the task periods of center arm and reward arm into early and
534 late epochs.
535
536 **Task performance depends on acetylcholine concentrations in the model**
537 In our model, two ACh-regulated mechanisms, that is, disinhibitory circuit in CA1 and
538 CAN current in MECV excitatory cells, play crucial roles in encoding, maintenance and
539 recall epochs of working memory tasks. Therefore, we examined whether these core
540 mechanisms work robustly when [ACh] is varied. We changed the default levels of
541 [ACh] with other parameter values unchanged. Lowering the default [ACh], which
542 weakens disinhibition, during the encoding epoch (sample-L) disenabled the CA1 L and
543 R subgroups to exhibit large enough activity differences to encode spatial information
544 in the CA1-MECV-MECIII loop circuit (Figure 6A, blue). Task performance was severely
545 impaired, contrasting to intact performance at higher default [ACh] levels (Figure 6B,

546 left). Lower default [ACh] levels during delay period had almost no effects on task
547 performance (Figure 6B, center). Finally, lower default [ACh] levels during the recall
548 epoch (test-C2) eliminated the reactivation of the subgroup L (Figure 6A, green) and
549 task performance was severely impaired (Figure 6B, right), but performance remained
550 intact at higher [ACh] levels. These results show that default [ACh] levels should be
551 sufficiently high during the encoding and recall epochs, but fine tuning of [ACh] is
552 unnecessary.
553
554 Next, we explored whether theta-phase-locked firing has anything to do with the
555 success of the working memory task. To this end, we compared the theta preference of
556 CA1 neurons during the test-C2 period between successful and failure trials in both
557 models and rats (Figure 6C). [ACh] was at the default levels. In both models and rats,
558 neurons preferentially fired around the peaks of theta oscillation in success trails, but
559 firing phases were somewhat delayed in failure trials.
560
561 **Figure 6. Cholinergic modulations in the network model.** (A) In CA1 (left) and MECIII
562 (right), differences in firing rate between the subgroups L and R were calculated at the
563 normal (black) and reduced levels of [ACh] during encoding (sample-C, blue) and recall
564 (test-C2, green) epochs. (B) Probability of left choice averaged over different networks
565 and initial conditions are shown at different levels of [ACh] during sample-L (left), delay
566 (center) and test-C2 (right) periods. Thick lines indicate results for the default [ACh]
567 levels. (C) Frequency of spikes in CA1 excitatory neurons during test-C2 periods (top)
568 are shown in the model (left) and rats (right). In the model, [ACh] was set to the
569 normal level and spike counts are shown separately for the subgroups L and C. Only the
570 total spike count is shown for rats. Bottom panels show the differences in firing rate
571 between successful and failure trials.
572
573 **Role of high-gamma oscillation in memory in MECIII and CA1**
574 Decision making in rats was accompanied by a rapid increase in coherent high-gamma
575 oscillations (60 -120 Hz) between MECIII and CA1 (Yamamoto et al., 2014). However,

we did not model the mechanism to generate prominent gamma oscillations to keep our model mathematically simple and minimal. Actually, the simplified mathematical description was sufficient for accounting for many findings on neural activity and rat behavior reported in the experiment. Then, the question arises about the role of coherent high gamma oscillation in the working memory task. To answer this question, we applied a common oscillatory input in the high-gamma range (80 Hz) to E neurons in MECIII and CA1 (Figure 7A: also see the STAR Methods). In the experiment, high gamma oscillations of LFPs were synchronized between MECIII and the lacunosum molecule layer of CA1, to which MECIII-to-CA1 connections project, indicating a common source of high gamma oscillations projecting to both areas.

High gamma oscillation improved the decoding of memorized information from the entorhinal-hippocampal loop circuit in the model. To show this, we built a virtual decoder of excitatory and inhibitory neurons receiving inputs from MECIII and CA1 (Figure 7A, see the STAR method for details). Stimulated by the high gamma input, E neurons in both areas tended to fire in the high-gamma frequency range (Figure7B). Spike bursts were delayed in CA1 by about 10 ms from those in MECIII, which is consistent with experimental observation (Yamamoto et al., 2014). Because this delay is approximately equal to the period of high gamma oscillation, synaptic inputs from the two areas coincidently arrived at the decoder in each high-gamma cycle. The coincident input amplified the evoked responses and facilitated spike firing of the decoder (see bursting of CA1, MECIII and decoder neurons around 7.7 sec in Figure 7B). In contrast, without the high gamma input, inputs from MECIII and CA1 did not arrive coherently to the decoder. Feedforward inhibition, which is a ubiquitously found motif of cortico-cortical synaptic connections (Isaacson and Scanziani, 2011), further attenuated the impact of incoherent spike input on decoder neurons. Thus, coherent high gamma activity in MECIII and CA1 may facilitate the readout of spatial information from MECIII by other cortical areas.

To generalize this observation, in Figure 7C, we quantified decoding performance while

606 changing burst size (the number of spikes per burst) in MECIII and CA1. The
607 performance was measured by the probability that coincident bursts in CA1 and MECIII
608 generate a spike burst in a decoder neuron. Without gamma oscillation, even a large
609 burst in MECIII and/or CA1 could not evoke a burst in the decoder. In contrast, in the
610 presence of gamma oscillation a small burst in MECIII and/or CA1 was sufficient for
611 evoking a burst in the decoder with high fidelity. These results further support the role
612 of coherent high gamma oscillation in facilitating the decoding performance. It is noted
613 that an increased high gamma coherence between CA1 and MECIII enhanced the
614 performance even if the input burst size was reduced.
615
616 **Figure 7. Role of high-gamma oscillation in information decoding.** (A) Decoding of
617 choice information from MECIII and CA1 is schematically illustrated. (B) Raster plots are
618 shown for CA1 and MECIII E neurons in the subgroup L and excitatory and inhibitory
619 neurons in the decoder. From 7.5 [s] to 8 [s], a common coherent high-gamma input
620 was applied to MECIII E and CA1 E neurons. (C) Decoding performance (upper) and the
621 average number of output spikes evoked from a decoder neuron by a single burst in
622 MECIII (left), CA1 (middle) or both (right) are plotted against the input burst size
623 (bottom). Spike counts obtained with (blue) and without (red) the high-gamma
624 oscillatory input are displayed. The decoding performance was defined as the
625 probability that the number of output spikes in a burst exceeds a threshold value
626 (dotted lines in bottom panels) for a given input burst size.
627
628
629 **Discussion**
630
631 In this study, we developed a model comprising MECV, MECIII and CA1 to explore how
632 these local circuits process and communicate information with each other during
633 DNMP tasks. Our model indicates that ACh concentration is modulated in a task-period
634 dependent manner to coordinate local network computation for encoding,
635 maintenance and recalling spatial information across the multiple cortical areas. With

636 these modulations, our model successfully replicates the various features of neural
637 activity observed in MECIII and CA1 (Yamamoto et al., 2014). In particular, the model
638 predicts that CA1 neurons change their preferred theta phases depending on cognitive
639 demands, which was also supported by experimental data (Fernández-Ruiz et al., 2017;
640 Mizuseki et al., 2013; Yamamoto et al., 2014).
641
642 **Relevance of MEC-CA1 loop to spatial working memory tasks**
643 The hippocampal area CA1 is a central locus for spatial information processing, and
644 stores the concurrent position of the rat (O'Keefe and Dostrovsky, 1971) as well as
645 retrospective and prospective representations of position information (Dragoi and
646 Buzsáki, 2006; Ferbinteanu and Shapiro, 2003; Foster and Wilson, 2006; Gupta et al.,
647 2010; Pastalkova et al., 2008; Zheng et al., 2016). Based on the hypothesis that the
648 CA1-MECV-MECIII loop circuit is involved in spatial working memory (van Strien et al.,
649 2009; Witter et al., 2000), we demonstrated how the spatial information of the
650 selected arm is encoded in CA1 during a sample trial (Figure 2), maintained in MECV
651 during delay period, and transferred to MECIII and reloaded on CA1 for decision
652 making (Figure 3). Consistent with the hypothesis, connections from MECIII to CA1 are
653 crucial for the success of spatial working memory tasks (Suh et al., 2011; Yamamoto et
654 al., 2014). Our model demonstrated this role of MECIII-to-CA1 connections in spatial
655 working memory, predicting their crucial contribution to memory encoding (Figure S3).
656 This prediction can be tested experimentally.
657
658 Sequence of spikes with theta phase precession, that is, "theta sequence" (Ferbinteanu
659 and Shapiro, 2003; Middleton and McHugh, 2016; Pfeiffer and Foster, 2013; Schlesiger
660 et al., 2015; Zheng et al., 2016), has been observed in the hippocampus and the MEC
661 during cognitive tasks requiring episodic memory. The blockade of MECIII-to-CA1
662 connections causes modulation of theta activity in MECIII (Suh et al., 2011; Yamamoto
663 et al., 2014). Similarly, inactivation of the MEC disrupts the temporal organization of
664 spikes and impairs information maintenance (Robinson et al., 2017). These results
665 imply that the temporal coordination of theta-phase-locked neuronal firing along the

CA1-MECV-MECIII loop circuit is crucial for the success of spatial working memory tasks. We showed an example case in which the disruption of this temporal coordination in MECIII led to a significant increase of failure trials (Figure S1B, C).

Our model hypothesizes that [ACh] changes in time during a working memory task, which generates shifts of preferred theta phase in CA1 E neurons: higher [ACh] advances the preferred phase towards the peak of theta oscillation (Figure 5). Based on this hypothesis, the model predicts that phase advances occur during the encoding epoch in sample trials (i.e., on the reward arm) and during the recall epoch in test trials (i.e., on the center arm). We validated this prediction with the results of two experiments (Fernández-Ruiz et al., 2017; Mizuseki et al., 2013; Yamamoto et al., 2014). Phase advances in the encoding epoch have been known previously and can be accounted for by temporal separation between CA3 input and MECIII input to CA1 (Colgin et al., 2009; Cutsuridis et al., 2010; Hasselmo et al., 2002; Lasztóczi and Klausberger, 2016; Milstein et al., 2015)(Mizuseki et al., 2009). Input from CA3 preferentially arrives at CA1 on the descending phase of theta oscillation of LFP (Klausberger and Somogyi, 2008) (Mizuseki et al., 2009)whereas input from MECIII arrives at the peaks of theta oscillation (Colgin et al., 2009; Fernández-Ruiz et al., 2017; Hasselmo et al., 2002) (Mizuseki et al., 2009). Because MECIII input, which presumably carries sensory information, seems to dominate CA3 input during encoding (Hasselmo2002), CA1 neurons likely fire at the peaks rather than the troughs of theta oscillation (Fernández-Ruiz et al., 2017).

Phase advances on the later central arm (i.e., in the recall epoch) represent a novel finding of this study. CA1 neurons were previously shown to fire at the troughs of theta oscillation during memory recall (Fernández-Ruiz et al., 2017), and this was consistent with the view that CA3 input dominates MECIII input during this epoch. Challenging the conventional view, our model predicts that CA1 neurons retrieve spatial memory from the MECIII, hence firing at the peaks of theta oscillation. Possibly consistent with this prediction, if we divide the center arm into early and late portions in (Mizuseki et al.,

2009), preferred theta phases show a second (and advanced) peak in the late portion of recall epoch (Figure 5D). This peak was absent in the previous analysis (Fernández-Ruiz et al., 2017) because the center arm was treated as a single entity. The consistency between the model and experiment requires further clarification.

Reflection of cognitive demands on the MEC-CA1 loop circuit through ACh

ACh is involved with several cognitive functions such as sensory discrimination (Hangya et al., 2015; Pinto et al., 2013), associative learning (Sabec et al., 2018), and spatial (Croxson et al., 2011; Okada et al., 2015) and non-spatial working memory (Furey et al., 2000; Hasselmo and Stern, 2006; McGaughy et al., 2005). In correlation with cognitive states, ACh concentration changes to modulate activity of the specific types of neurons (Muñoz et al., 2017; Womelsdorf et al., 2014) through muscarinic and nicotinic receptors (Parikh et al., 2007; Teles-Grilo Ruivo et al., 2017; Zhang et al., 2010). In associative learning, ACh was suggested to facilitate MECIII-to-CA1 input during the encoding epoch and CA3-to-CA1 input during the decoding epoch (Hasselmo, 2006). We propose a novel role and mechanism of ACh for the functions of the entorhinal-hippocampal loop circuit according to the cognitive demands arising during a spatial working memory task, namely, memory encoding, maintenance and recall. Consistent with the proposal of our model (Figure 1D), it has recently been shown in a DNMP task (Teles-Grilo Ruivo et al., 2017) that [ACh] is significantly higher on the reward arm than in other positions in both sample and test trials, that on the center arm [ACh] tends to be larger in test trials than in sample trials, and that [ACh] is low in delay periods (c.f., Figure 6B).

We assumed that a change in cognitive demands is reflected in a phasic change in [ACh] on the timescale of seconds. However, [ACh] is thought to change in a diffusive and tonic manner on much slower timescales of minutes or hours. Importantly, recent studies have revealed that [ACh] undergoes phasic changes at sub-second and second timescales (Parikh et al., 2007; Teles-Grilo Ruivo et al., 2017; Zhang et al., 2010), and such a phasic change in [ACh] is associated with reward or aversive signals (Hangya et

726 al., 2015). Further, task performance is correlated with slower tonic increases in [ACh]
727 during the task period (Parikh et al., 2007), but uncorrelated with phasic changes in
728 [ACh] in the reward arm (Teles-Grilo Ruivo et al., 2017). In our model, task performance
729 saturates above a certain level of [ACh] in the reward arm (Left panel in Figure 6B). Our
730 results suggest that the tonic level of [Ach] expresses an overall bias during each trial
731 and a phasic increase in [Ach] gives a more elaborate modulation reflecting a specific
732 cognitive demand.
733
734 **Dynamic processing across multiple areas**
735 Coherence in neural activity between different cortical areas varies with the cognitive
736 state of the brain (Benchenane et al., 2010; Fries, 2015). Furthermore, disruption of a
737 cortico-cortical interaction at different behavioral states can impair task performance
738 differently (Spellman et al., 2015; Yamamoto et al., 2014). These results imply that
739 information flows between cortical areas are differentially routed according to the
740 demand of the on-going cognitive process through the dynamical regulation of
741 corticocortical coherence. Theoretical studies have proposed several mechanisms of
742 information routing based on a balance control between excitatory and inhibitory
743 synaptic inputs (Vogels and Abbott, 2009), disinhibitory circuits (Yang et al., 2016),
744 spontaneous bursts (Palmigiano et al., 2017), and band-pass filtering by a feed-forward
745 inhibitory circuit (Akam and Kullmann, 2010). While these studies focused on the
746 circuit mechanisms of information routing, we addressed how such mechanisms are
747 integrated to perform a spatial working memory task through different cognitive
748 demands (Benchenane et al., 2010; Spellman et al., 2015; Yamamoto et al., 2014). We
749 demonstrated that cholinergic inputs coordinate the encoding and recall functions by
750 modulating the cortical disinhibitory circuit and Ca^{2+}-dependent cationic channels in
751 excitatory cells.
752
753 Accumulating evidence suggests that disinhibitory circuits play a crucial role in
754 cognitive tasks such as fear conditioning (Letzkus et al., 2011; Pi et al., 2013) and
755 sensory discrimination (Hangya et al., 2015; Pinto et al., 2013). VIP, SOM and PV

inhibitory neurons are dominant interneuron types of the disinhibitory circuit (Donato et al., 2013; Francavilla et al., 2018; Kamigaki and Dan, 2017; Zhang et al., 2014) VIP neurons express muscarinic receptors and are depolarized by cholinergic input (Bell et al., 2014). VIP neurons project more strongly to SOM neurons than to PV neurons in cortical areas (Kamigaki and Dan, 2017; Zhang et al., 2014), but some studies have shown stronger modulations of PV neurons in the hippocampus (Donato et al., 2013; Francavilla et al., 2018). PV neurons innervating the perisomatic area of CA1 excitatory neurons preferably spike in the descending phase of theta oscillation (Klausberger and Somogyi, 2008) to weaken CA3 input. In contrast, SOM (OLM in CA1) neurons projecting the distal dendrites of CA1 excitatory neurons preferably spike at the troughs of theta oscillation (Klausberger and Somogyi, 2008)(Royer et al. Buzskai, 2012 Nature Neuroscience) to weaken MECIII input. Because MECIII input rarely arrive at the troughs of theta oscillation, the suppression of MECIII input by disinhibited OLM neurons exerts a smaller effect on excitatory neuron firing compared to disinhibited PV neurons. Therefore, we mainly focused on the effect of PV neurons on neural circuit functions. In line with our model's prediction (Figure S2), optogenetic inhibition of PV neurons impairs performance in spatial working memory (Murray et al., 2011). However, the actual spikes delivered by the MECIII are distributed broadly over a theta cycle in rats (Mizuseki et al., 2009), implying that disinhibition of PV and SOM neurons can modulate activity of excitatory neurons in parallel. Indeed, our model predicts that inactivation of PV or VIP neurons impairs task performance in different ways (Figure S2). This prediction can be examined by a selective inhibition of either neuron types in the spatial working memory task.

Covert memory state for maintenance of information

Recent studies showed that dynamically evolving neuronal activity can maintain information during a delay period in working memory tasks (Murray et al., 2017; Stokes, 2015; Wolff et al., 2017)(Pastalkova et al., 2008). In the DNMP task we studied (Yamamoto et al., 2014), theta phase-locked firing of MECIII neurons was correlated with the success of the task. Nevertheless, this neuronal activity temporarily vanished

786 during a delay period, implying that a non-spiking activity maintains information on the
787 previous choice. We hypothesized that the conductance of a specific ionic channel, i.e.,
788 calcium-dependent cationic current, remains in an elevated state to preserve spatial
789 information during delay period. This elevated state is not accompanied by neuronal
790 firing, hence is consistent with experimental observations. This mechanism was
791 originally proposed to account for persistent activity of isolated single neurons
792 (Fransen et al., 2002; Fransén et al., 2006) and suggested to be engaged in temporal
793 association memory (Kitamura et al., 2014). Our model demonstrates that the same
794 mechanism can generate a covert memory state necessary in spatial working memory.
795 This and other mechanisms of covert memory state, for instance, short-term synaptic
796 plasticity (Mongillo et al., 2008), are not mutually exclusive. However, our mechanism
797 has an important advantage that working memory maintenance is turned on and off
798 by cholinergic modulation depending on the cognitive demand. Thus, our results
799 suggest that neuromodulators are crucial for the flexible control of memory processing
800 by the brain.
801
802 **Limitation of the model**
803 We showed that coherent activations of CA1 and MECIII at high-gamma frequencies
804 facilitate decoding of information about the previous choice from CA1 and MECIII
805 (Figure 7). However, gamma oscillation is not absolutely necessary in our model for
806 performing spatial working memory tasks. Theta-phase-locked neuronal firing alone
807 could sufficiently facilitate information transfer along the MECIII-CA1-MECV loop circuit
808 without gamma oscillation. This result may somewhat contradict the experimentally
809 suggested role of gamma oscillation in information transfer between the hippocampus
810 and entorhinal cortex (Colgin et al., 2009; Yamamoto et al., 2014). The role of gamma
811 oscillation needs to be further explored.
812
813 Secondly, we did not model any mechanism to translate the decoded information into
814 a correct choice behavior under a given rule of decision making (e.g., the alternate
815 choice of left or right turn). The mPFC is projected to by CA1 and projects back to it via

reuniens (Dolleman-Van Der Weel and Witter, 1996; Ito et al., 2015), and is engaged in spatial working memory (Bolkan et al., 2017; Jones and Wilson, 2005; Spellman et al., 2015). Furthermore, some mPFC neurons exhibit rule-related activities. However, the delay-period activity of mPFC neurons is specific to neither previous nor present location in a DNMP task (Bolkan2017) and the rule-related activities are not location-specific (Durstewitz et al., 2010; Guise and Shapiro, 2017; Preston and Eichenbaum, 2013). Where and how decision rules are processed and how spatial working memory and rule-related activities are integrated are open to future studies.

References

Akam, T.E., and Kullmann, D.M. (2010). Oscillations and Filtering Networks Support Flexible Routing of Information. Neuron *67*, 308–320.

Albuquerque, E.X., Pereira, E.F.R., Alkondon, M., and Rogers, S.W. (2009). Mammalian Nicotinic Acetylcholine Receptors: From Structure to Function. Physiol. Rev. *89*, 73–120.

Bell, L.A., Bell, K. a, and McQuiston, a R. (2014). Activation of muscarinic receptors by ACh release in hippocampal CA1 depolarizes VIP but has varying effects on parvalbumin-expressing basket cells. J. Physiol. *1*, 197–215.

Benchenane, K., Peyrache, A., Khamassi, M., Tierney, P.L., Gioanni, Y., Battaglia, F.P., and Wiener, S.I. (2010). Coherent Theta Oscillations and Reorganization of Spike Timing in the Hippocampal- Prefrontal Network upon Learning. Neuron *66*, 921–936.

Bittner, K.C., Grienberger, C., Vaidya, S.P., Milstein, A.D., Macklin, J.J., Suh, J., Tonegawa, S., and Magee, J.C. (2015). Conjunctive input processing drives feature selectivity in hippocampal CA1 neurons. Nat. Neurosci. *18*, 1–13.

Bolkan, S.S., Stujenske, J.M., Parnaudeau, S., Spellman, T.J., Rauffenbart, C., Abbas, A.I., Harris, A.Z., Gordon, J.A., and Kellendonk, C. (2017). Thalamic projections sustain prefrontal activity during working memory maintenance. Nat. Neurosci. *20*, 987–996.

Borhegyi, Z. (2004). Phase Segregation of Medial Septal GABAergic Neurons during Hippocampal Theta Activity. J. Neurosci. *24*, 8470–8479.

Buehlmann, A., and Deco, G. (2010). Optimal Information Transfer in the Cortex

846 through Synchronization. PLoS Comput. Biol. *6*, e1000934.
847 Colgin, L.L., Denninger, T., Fyhn, M., Hafting, T., Bonnevie, T., Jensen, O., Moser, M.-B.,
848 and Moser, E.I. (2009). Frequency of gamma oscillations routes flow of information in
849 the hippocampus. Nature *462*, 353–357.
850 Croxson, P.L., Kyriazis, D.A., and Baxter, M.G. (2011). Cholinergic modulation of a
851 specific memory function of prefrontal cortex. Nat. Neurosci. *14*, 1510–1512.
852 Cutsuridis, V., Cobb, S., and Graham, B.P. (2010). Encoding and retrieval in a model of
853 the hippocampal CA1 microcircuit. Hippocampus *20*, 423–446.
854 Dolleman-Van Der Weel, M., and Witter, M.P. (1996). Projections From the Nucleus
855 Reuniens Thalami to the Entorhinal Cortex , Hippocampal Field CA1 , and the
856 Subiculum in the Rat Arise From Different Populations of Neurons. J. Comp. Neurol.
857 *364*, 637–650.
858 Donato, F., Rompani, S.B., and Caroni, P. (2013). Parvalbumin-expressing basket-cell
859 network plasticity induced by experience regulates adult learning. Nature *504*, 272–
860 276.
861 Dragoi, G., and Buzsáki, G. (2006). Temporal encoding of place sequences by
862 hippocampal cell assemblies. Neuron *50*, 145–157.
863 Durstewitz, D., Vittoz, N.M., Floresco, S.B., and Seamans, J.K. (2010). Abrupt transitions
864 between prefrontal neural ensemble states accompany behavioral transitions during
865 rule learning. Neuron *66*, 438–448.
866 Eichenbaum, H. (2017). Prefrontal – hippocampal interactions in episodic memory.
867 Nat. Publ. Gr. *18*, 547–558.
868 Ferbinteanu, J., and Shapiro, M.L. (2003). Prospective and Retrospective Memory
869 Coding in the Hippocampus. Neuron *40*, 1227–1239.
870 Fernández-Ruiz, A., Oliva, A., Nagy, G.A., Maurer, A.P., Berényi, A., and Buzsáki, G.
871 (2017). Entorhinal-CA3 Dual-Input Control of Spike Timing in the Hippocampus by
872 Theta-Gamma Coupling. Neuron *93*, 1213–1226.e5.
873 Foster, D.J., and Wilson, M.A. (2006). Reverse replay of behavioural sequences in
874 hippocampal place cells during the awake state. Nature *440*, 680–683.
875 Francavilla, R., Villette, V., Luo, X., Chamberland, S., Muñoz-Pino, E., Camiré, O.,

876 Wagner, K., Kis, V., Somogyi, P., and Topolnik, L. (2018). Connectivity and network
877 state-dependent recruitment of long-range VIP-GABAergic neurons in the mouse
878 hippocampus. Nat. Commun. *9*, 5043.
879 Fransen, E., Alonso, A.A., and Hasselmo, M.E. (2002). Simulations of the role of the
880 muscarinic-activated calcium-sensitive nonspecific cation current INCM in entorhinal
881 neuronal activity during delayed matching tasks. J. Neurosci. *22*, 1081–1097.
882 Fransén, E., Tahvildari, B., Egorov, A. V, Hasselmo, M.E., and Alonso, A. a (2006).
883 Mechanism of graded persistent cellular activity of entorhinal cortex layer v neurons.
884 Neuron *49*, 735–746.
885 Fries, P. (2015). Rhythms for Cognition: Communication through Coherence. Neuron
886 *88*, 220–235.
887 Furey, M.L., Pietrini, P., and Haxby, J. V (2000). Cholinergic enhancement and increased
888 selectivity of perceptual processing during working memory. Science *290*, 2315–2319.
889 Gonzalez-Sulser, A., Parthier, D., Candela, A., McClure, C., Pastoll, H., Garden, D.,
890 Surmeli, G., and Nolan, M.F. (2014). GABAergic Projections from the Medial Septum
891 Selectively Inhibit Interneurons in the Medial Entorhinal Cortex. J. Neurosci. *34*,
892 16739–16743.
893 Guise, K.G., and Shapiro, M.L. (2017). Medial Prefrontal Cortex Reduces Memory
894 Interference by Modifying Hippocampal Encoding. Neuron *94*, 183–192.e8.
895 Gupta, A.S., van der Meer, M.A.A., Touretzky, D.S., and Redish, A.D. (2010).
896 Hippocampal Replay Is Not a Simple Function of Experience. Neuron *65*, 695–705.
897 Hangya, B., Ranade, S.P., Lorenc, M., and Kepecs, A. (2015). Central Cholinergic
898 Neurons Are Rapidly Recruited by Reinforcement Feedback. Cell *162*, 1155–1168.
899 Hasselmo, M.E. (2006). The role of Acetylcholine in learning and memory. Curr. Opin.
900 Neurobiol. *16*.
901 Hasselmo, M.E., and Sarter, M. (2010). Modes and Models of Forebrain Cholinergic
902 Neuromodulation of Cognition. Neuropsychopharmacology *36*, 52–73.
903 Hasselmo, M.E., and Stern, C.E. (2006). Mechanisms underlying working memory for
904 novel information. Trends Cogn. Sci. *10*, 487–493.
905 Hasselmo, M.E., Bodelón, C., and Wyble, B.P. (2002). A proposed function for

hippocampal theta rhythm: separate phases of encoding and retrieval enhance reversal of prior learning. Neural Comput. *14*, 793–817.

Isaacson, J.S., and Scanziani, M. (2011). How inhibition shapes cortical activity. Neuron *72*, 231–243.

Ito, H.T., Zhang, S., Witter, M.P., Moser, E.I., and Moser, M. (2015). A prefrontal–thalamo–hippocampal circuit for goal-directed spatial navigation. Nature *522*, 50–55.

Jones, M.W., and Wilson, M.A. (2005). Theta Rhythms Coordinate Hippocampal–Prefrontal Interactions in a Spatial Memory Task. PLoS Biol. *3*, e402.

Kamigaki, T., and Dan, Y. (2017). Delay activity of specific prefrontal interneuron subtypes modulates memory-guided behavior. Nat. Neurosci. *20*, 854–863.

Kitamura, T., Pignatelli, M., Suh, J., Kohara, K., Yoshiki, A., Abe, K., and Tonegawa, S. (2014). Island Cells Control Temporal Association Memory. Science (80-.). *343*, 896–901.

Klausberger, T., and Somogyi, P. (2008). Neuronal diversity and temporal dynamics: the unity of hippocampal circuit operations. Science *321*, 53–57.

Lasztóczi, B., and Klausberger, T. (2016). Hippocampal Place Cells Couple to Three Different Gamma Oscillations during Place Field Traversal. Neuron *91*, 34–40.

Letzkus, J.J., Wolff, S.B.E., Meyer, E.M.M., Tovote, P., Courtin, J., Herry, C., and Lüthi, A. (2011). A disinhibitory microcircuit for associative fear learning in the auditory cortex. Nature *480*, 331–335.

Letzkus, J.J., Wolff, S.B.E., and Lüthi, A. (2015). Disinhibition, a Circuit Mechanism for Associative Learning and Memory. Neuron *88*, 264–276.

Masamizu, Y., Tanaka, Y.R., Tanaka, Y.H., Hira, R., Ohkubo, F., Kitamura, K., Isomura, Y., Okada, T., and Matsuzaki, M. (2014). Two distinct layer-specific dynamics of cortical ensembles during learning of a motor task. Nat. Neurosci. *17*, 987–994.

McGaughy, J., Koene, R.A., Eichenbaum, H., and Hasselmo, M.E. (2005). Cholinergic Deafferentation of the Entorhinal Cortex in Rats Impairs Encoding of Novel But Not Familiar Stimuli in a Delayed Nonmatch-to-Sample Task. J. Neurosci. *25*, 10273–10281.

Middleton, S.J., and McHugh, T.J. (2016). Silencing CA3 disrupts temporal coding in the CA1 ensemble. Nat. Neurosci. *19*, 945–951.

936 Middleton, S., Jalics, J., Kispersky, T., Lebeau, F.E.N., Roopun, A.K., Kopell, N.J.,
937 Whittington, M.A., and Cunningham, M.O. (2008). NMDA receptor-dependent
938 switching between different gamma rhythm-generating microcircuits in entorhinal
939 cortex. Proc. Natl. Acad. Sci. U. S. A. *105*, 18572–18577.
940 Milstein, A.D., Bloss, E.B., Apostolides, P.F., Vaidya, S.P., Dilly, G.A., Zemelman, B. V,
941 and Magee, J.C. (2015). Inhibitory Gating of Input Comparison in the CA1 Microcircuit.
942 Neuron *87*, 1274–1289.
943 Mizuseki, K., Sirota, A., Pastalkova, E., and Buzsáki, G. (2009). Theta Oscillations
944 Provide Temporal Windows for Local Circuit Computation in the Entorhinal-
945 Hippocampal Loop. Neuron *64*, 267–280.
946 Mizuseki, K., Sirota, A., Pastalkova, E., Diba, K., and Buzsaki, G. (2013). Multiple single
947 unit recordings from different rat hippocampal and entorhinal regions while the
948 animals were performing multiple behavioral tasks.
949 Mongillo, G., Barak, O., and Tsodyks, M. (2008). Synaptic theory of working memory.
950 Science *319*, 1543–1546.
951 Muñoz, W., Tremblay, R., Levenstein, D., and Rudy, B. (2017). Layer-specific
952 modulation of neocortical dendritic inhibition during active wakefulness. Science (80-
953 .). *355*, 954–959.
954 Murray, A.J., Sauer, J.-F., Riedel, G., McClure, C., Ansel, L., Cheyne, L., Bartos, M.,
955 Wisden, W., and Wulff, P. (2011). Parvalbumin-positive CA1 interneurons are required
956 for spatial working but not for reference memory. Nat. Neurosci. *14*, 297–299.
957 Murray, J.D., Bernacchia, A., Roy, N.A., Constantinidis, C., Romo, R., and Wang, X.-J.
958 (2017). Stable population coding for working memory coexists with heterogeneous
959 neural dynamics in prefrontal cortex. Proc. Natl. Acad. Sci. *114*, 394–399.
960 Newman, E.L., Gupta, K., Climer, J.R., Monaghan, C.K., and Hasselmo, M.E. (2012).
961 Cholinergic modulation of cognitive processing: insights drawn from computational
962 models. Front. Behav. Neurosci. *6*, 1–19.
963 O'Keefe, J., and Dostrovsky, J. (1971). The hippocampus as a spatial map. Preliminary
964 evidence from unit activity in the freely-moving rat. Brain Res. *34*, 171–175.
965 Okada, K., Nishizawa, K., Kobayashi, T., Sakata, S., and Kobayashi, K. (2015). Distinct

roles of basal forebrain cholinergic neurons in spatial and object recognition memory. Sci. Rep. *5*, 13158.

Palmigiano, A., Geisel, T., Wolf, F., and Battaglia, D. (2017). Flexible information routing by transient synchrony. Nat. Neurosci. *20*, 1014–1022.

Parikh, V., Kozak, R., Martinez, V., and Sarter, M. (2007). Prefrontal Acetylcholine Release Controls Cue Detection on Multiple Timescales. Neuron *56*, 141–154.

Pastalkova, E., Itskov, V., Amarasingham, A., and Buzsaki, G. (2008). Internally Generated Cell Assembly Sequences in the Rat Hippocampus. Science (80-.). *321*, 1322–1327.

Pfeiffer, B.E., and Foster, D.J. (2013). Hippocampal place-cell sequences depict future paths to remembered goals. Nature *497*, 74–79.

Pi, H.-J., Hangya, B., Kvitsiani, D., Sanders, J.I., Huang, Z.J., and Kepecs, A. (2013). Cortical interneurons that specialize in disinhibitory control. Nature *503*, 521–524.

Pinto, L., Goard, M.J., Estandian, D., Xu, M., Kwan, A.C., Lee, S., Harrison, T.C., Feng, G., and Dan, Y. (2013). Fast modulation of visual perception by basal forebrain cholinergic neurons. Nat. Publ. Gr. *16*, 1857–1863.

Preston, A.R., and Eichenbaum, H. (2013). Interplay of hippocampus and prefrontal cortex in memory. Curr. Biol. *23*, 764–773.

Rahman, J., and Berger, T. (2011). Persistent activity in layer 5 pyramidal neurons following cholinergic activation of mouse primary cortices. Eur. J. Neurosci. *34*, 22–30.

Robinson, N.T.M., Priestley, J.B., Rueckemann, J.W., Garcia, A.D., Smeglin, V.A., Marino, F.A., and Eichenbaum, H. (2017). Medial Entorhinal Cortex Selectively Supports Temporal Coding by Hippocampal Neurons. Neuron *94*, 677–688.e6.

Rotstein, H.G., Oppermann, T., White, J.A., and Kopell, N.J. (2006). The dynamic structure underlying subthreshold oscillatory activity and the onset of spikes in a model of medial entorhinal cortex stellate cells. J. Comput. Neurosci. *21*, 271–292.

Sabec, M.H., Wonnacott, S., Warburton, E.C., and Bashir, Z.I. (2018). Nicotinic Acetylcholine Receptors Control Encoding and Retrieval of Associative Recognition Memory through Plasticity in the Medial Prefrontal Cortex. Cell Rep. *22*, 3409–3415.

Schlesiger, M.I., Cannova, C.C., Boublil, B.L., Hales, J.B., Mankin, E.A., Brandon, M.P.,

Leutgeb, J.K., Leibold, C., and Leutgeb, S. (2015). The medial entorhinal cortex is necessary for temporal organization of hippocampal neuronal activity. Nat. Neurosci. *18*.

Spellman, T., Rigotti, M., Ahmari, S.E., Fusi, S., Gogos, J.A., and Gordon, J.A. (2015). Hippocampal–prefrontal input supports spatial encoding in working memory. Nature *522*, 309–314.

Stokes, M.G. (2015). 'Activity-silent' working memory in prefrontal cortex: a dynamic coding framework. Trends Cogn. Sci. *19*, 394–405.

van Strien, N.M., Cappaert, N.L.M., and Witter, M.P. (2009). The anatomy of memory: an interactive overview of the parahippocampal–hippocampal network. Nat. Rev. Neurosci. *10*, 272–282.

Suh, J., Rivest, A.J., Nakashiba, T., Tominaga, T., and Tonegawa, S. (2011). Entorhinal Cortex Layer III Input to the Hippocampus Is Crucial for Temporal Association Memory. Science (80-.). *334*, 1415–1420.

Swanson, L.W., and Cowan, W.M. (1977). An Autoradiographic Study of the Organization of the Efferent Connections of the Hippocampal Formation in the Rat. J. Comp. Neurol. *172*, 49–84.

Takahashi, H., and Magee, J.C. (2009). Pathway Interactions and Synaptic Plasticity in the Dendritic Tuft Regions of CA1 Pyramidal Neurons. Neuron *62*, 102–111.

Teles-Grilo Ruivo, L.M., Baker, K.L., Conway, M.W., Kinsley, P.J., Gilmour, G., Phillips, K.G., Isaac, J.T.R., Lowry, J.P., and Mellor, J.R. (2017). Coordinated Acetylcholine Release in Prefrontal Cortex and Hippocampus Is Associated with Arousal and Reward on Distinct Timescales. Cell Rep. *18*, 905–917.

Unal, G., Joshi, A., Viney, T.J., Kis, V., and Somogyi, P. (2015). Synaptic Targets of Medial Septal Projections in the Hippocampus and Extrahippocampal Cortices of the Mouse. J. Neurosci. *35*, 15812–15826.

Vogels, T.P., and Abbott, L.F. (2005). Signal propagation and logic gating in networks of integrate-and-fire neurons. J. Neurosci. *25*, 10786–10795.

Vogels, T.P., and Abbott, L.F. (2009). Gating multiple signals through detailed balance of excitation and inhibition in spiking networks. Nat. Neurosci. *12*, 483–491.

Wang, X.-J., and Buzsáki, G. (1996). Gamma oscillation by synaptic inhibition in a hippocampal interneuronal network model. J. Neurosci. *16*, 6402–6413.

Witter, M.P., Wouterlood, F.G., Naber, P.A., and Van Haeften, T. (2000). Anatomical organization of the parahippocampal-hippocampal network. Ann. N. Y. Acad. Sci. *911*, 1–24.

Wolff, M.J., Jochim, J., Akyürek, E.G., and Stokes, M.G. (2017). Dynamic hidden states underlying working-memory-guided behavior. Nat. Neurosci.

Womelsdorf, T., Valiante, T. a, Sahin, N.T., Miller, K.J., and Tiesinga, P.H. (2014). Dynamic circuit motifs underlying rhythmic gain control, gating and integration. Nat. Neurosci. *17*, 1031–1039.

Wulff, P., Ponomarenko, A. a, Bartos, M., Korotkova, T.M., Fuchs, E.C., Bähner, F., Both, M., Tort, A.B.L., Kopell, N.J., Wisden, W., et al. (2009). Hippocampal theta rhythm and its coupling with gamma oscillations require fast inhibition onto parvalbumin-positive interneurons. Proc. Natl. Acad. Sci. U. S. A. *106*, 3561–3566.

Yamamoto, J., Suh, J., Takeuchi, D., and Tonegawa, S. (2014). Successful Execution of Working Memory Linked to Synchronized High-Frequency Gamma Oscillations. Cell *157*, 845–857.

Yang, G.R., Murray, J.D., and Wang, X. (2016). A dendritic disinhibitory circuit mechanism for pathway-specific gating. Nat. Commun. *7*, 12815.

Zhang, H., Lin, S.-C., and Nicolelis, M. a L. (2010). Spatiotemporal coupling between hippocampal acetylcholine release and theta oscillations in vivo. J. Neurosci. *30*, 13431–13440.

Zhang, S., Xu, M., Kamigaki, T., Hoang Do, J.P., Chang, W.-C., Jenvay, S., Miyamichi, K., Luo, L., and Dan, Y. (2014). Long-range and local circuits for top-down modulation of visual cortex processing. Science (80-.). *345*, 660–665.

Zheng, C., Bieri, K.W., Hsiao, Y., and Colgin, L.L. (2016). Spatial Sequence Coding Differs during Slow and Fast Gamma Rhythms in the Hippocampus. Neuron *89*, 398–408.

STAR Methods

Neuron models

Our model has two classes of neurons: i) Poisson neurons; ii) Hodgkin-Huxley type (HH) neurons.

i) Poisson neurons

There are four types of theta-oscillating neurons (excitatory neurons in CA3 and MECII, VIP neurons in CA1 and GABAergic neurons in MS) and noise neurons. Other types of neurons, that is, excitatory (E) neurons, fast spiking (PV) neurons and OLM neurons in CA1, E and PV neurons in MECIII and E and PV neurons in MECV, are modeled as HH neurons. 40 excitatory and 40 inhibitory noise neurons project to all HH neurons. Firing rates of noise neurons are different depending on the cortical areas modeled: 35 [Hz] in CA1 and in MECIII and 30 [Hz] in MECV.

For theta-oscillating Poisson neurons, we described the theta-oscillating (10Hz) probability of spiking per unit time $P_x(t_1 < t < t_1 + \Delta t)$ (x=E in CA3 and MECII, VIP in CA1, GABA in MS) as

$$P_x(t_1 < t < t_1 + \Delta t) = (\Theta(A_x\left(sin\left(2\pi\left(\frac{t}{T} - \theta_x\right)\right) + B_x\right)) + C_x)\Delta t,$$

where $\Theta(s) = s$ when $s>0$ or otherwise 0. $T = 100$ ms and Δt = 0.02 ms is the step size of our numerical simulation. A_x and B_x are the amplitude and preferred phase of oscillating firing rate, respectively, and θ_x is the preferred phase of theta oscillation for the neuron type x, whereas C_x is the amplitude of background noise for inactive subgroups outside of their place fields. We set the preferred phases based on previous experimental studies (Borhegyi, 2004; Klausberger and Somogyi, 2008; Mizuseki et al., 2009) as follows:

x = CA3:

CA3 neurons in the model are divided into four groups according to their spatial preferences (Figure 1 and Circuit structure in STAR Methods). Their firing patterns are changed depending on the present location of the model rat. When the model rat is in Center ($0 < t < 1000$ ms, sample-C and $4500 \leq t < 7500$ ms, test-C), sample-Left ($1000 \leq t < 3000$ ms) and Home ($3000 \leq t < 4500$ms) positions, Center, Left, and Home subgroups are activated, respectively.

$$A_x = 30\ [\mathrm{Hz}], B_x = 1, C_x = 0\ [\mathrm{Hz}], \theta_x = -0.2$$

for neurons in an active subgroup, and

$$A_x = 0\ [\mathrm{Hz}], C_x = 3\ [\mathrm{Hz}]$$

for neurons in inactive subgroups.

x = ECII:

During the entire trial period, we set the parameters as

$$A_x = 5\ [\mathrm{Hz}], B_x = 0.6, C_x = 0\ [\mathrm{Hz}], \theta_x = -0.2$$

x = GABAergic in MS:

Three groups exist in the model, those projecting to PV in CA1, to OLM in CA1 and to PV in MECV. The preferred theta phase of MECV PV-projecting GABAergic neurons is the same as that of CA1 OLM-projecting GABAergic neurons,

$$A_x = 5[Hz], B_x = 0.8, C_x = 0[Hz], \theta_x = -0.1,$$

whereas the preferred phases of CA1 PV-projecting neurons are different from the above ones (Borhegyi, 2004) and given by

$$A_x = 5[\mathrm{Hz}], B_x = 2.0, C_x = 0[Hz], \theta_x = -0.5.$$

x=VIP:

During the entire trial period, we set the parameters as

$$A_x = 20[Hz], B_x = 0.3, C_x = 0[Hz], \theta_x = -0.4.$$

Finally, we set a reference theta oscillation in CA1 SP as

$$A_x = 1, \theta_x = 0.5, B_x = 0, C_x = 0,$$

which is a virtual oscillatory component used only for determining the relative oscillation phases of other brain regions to theta oscillation in CA1 SP, but not for numerically simulating the network model.

ii) HH neurons

In our model, there are seven types of neurons; E, PV and OLM in CA1, and E and PV in MECV and MECIII. PV neurons are modeled identically in all areas (Wang and Buzsáki, 1996). In the following equations, I_i is synaptic input from other neurons as described in Circuit structure in STAR Methods. Dynamics of each type of neurons is described below.

a) Excitatory neurons in CA1

We modeled excitatory neurons in CA1 based on (Wulff et al., 2009). We additionally included an afterhyperpolarization (AHP) and h currents in the model for generating a weak subthreshold oscillation of the membrane potentials through interplay between AHP (Middleton et al., 2008) and h current (Rotstein et al., 2006).

$$V_{Na} = 50[mV], V_K = -100.0[mV], V_{AHP} = -100.0[mV], V_h = -20.0[mV], V_L = -67.0[mV]$$

$$g_{Na} = 100.0[mS/cm^2], g_K = 80.0[mS/cm^2], g_{AHP} = 0.2[mS/cm^2], g_h = 0.1[mS/cm^2], g_L = 0.1[mS/cm^2]$$

$$C = 1, I_{cnst} = -0.1$$

$$C\frac{dV_i}{dt} = g_{Na}m_\infty(V)^3h(V_{Na}-V_i) + g_K n^4(V_K - V_i) + g_{AHP}w(V_{AHP}-V_i)$$
$$+ g_h(0.65hf + 0.35hs)(V_h - V_i) + g_L(V_L - V_i) + I_i + I_{const}$$

The channel variable h is determined as

$$h = \max(1 - 1.25n, 0).$$

Other channel variables evolve according to

$$\frac{dx}{dt} = \frac{x_\infty(V) - x}{\tau_x(V)},$$

where *x* = *m*, *n*, *w*, *hf* and *hs*. Among these variables, *m* and *n* are determined by

$$x_\infty(V) = \frac{\alpha_x(V)}{\alpha_x(V)+\beta_x(V)},$$
$$\tau_x(V) = 1/(\alpha_x(V) + \beta_x(V)),$$

where *x* stands for either *m* or *n*, and

$$\alpha_m(V) = -0.32(V+54)/(\exp(-0.25*(V+54)) - 1,.$$
$$\beta_m(V) = 0.28(V+27)/(\exp(0.2*(V+27)) - 1),$$
$$\alpha_n(V) = -0.032(V+52)/(\exp(-0.2*(V+52)) - 1),$$
$$\beta_n(V) = 0.5\exp(-0.025(V+57)).$$

Other variables are determined by

$$w_\infty(V) = \frac{1}{\exp(-0.1(V+41)) + 1}$$
$$\tau_w(V) = \frac{500}{3.3\exp(0.05(V+41)) + \exp(-0.05(V+41))}$$
$$hf_\infty(V) = 1/(1 + \exp\left(\frac{V+79.2}{9.78}\right))$$
$$\tau_{hf}(V) = \frac{0.51}{\exp((V-1.7)/10) + \exp(-(V+340)/52)} + 1$$
$$hs_\infty(V) = 1/\left(1 + \exp\left(\frac{V+2.83}{15.9}\right)\right)^{58}$$
$$\tau_{hs}(V) = \frac{5.6}{\exp\left(\frac{V-1.7}{14}\right) + \exp\left(\frac{-(V+260)}{43}\right)} + 1.$$

b) PV in CA1, MECIII, MECV

We modeled PV neurons in CA1 as well as those in MECIII and MECV as described in (Wang and Buzsáki, 1996).

$$V_{Na} = 55[mV], V_K = -90.0[mV], V_L = -65.0[mV]$$
$$g_{Na} = 35.0[mS/cm^2], g_K = 9.0[mS/cm^2], g_L = 0.1[mS/cm^2]$$
$$C = 1$$
$$C\frac{dV_i}{dt} = g_{Na}m_\infty(V)^3h(V_{Na}-V_i) + g_K n^4(V_K - V_i) + g_L(V_L - V_i) + I_i$$

$$\frac{dx}{dt} = \frac{x_\infty(V) - x}{\tau_x(V)}$$

$$x_\infty(V) = \frac{\alpha_x(V)}{\alpha_x(V) + \beta_x(V)}$$

$$\tau_x(V) = 1/(\alpha_x(V) + \beta_x(V)),$$

where the index $x = n$, h and m.

$$\alpha_m(V) = 0.1(V + 35)/(1 - \exp(-0.1(V + 35))$$

$$\beta_m(V) = 4\exp(-\frac{V + 57}{40})$$

$$\alpha_n(V) = 0.01(V + 34)/(1 - \exp(-(V + 34)))$$

$$\beta_n(V) = 0.125\exp(-(V + 44)/80)$$

$$\alpha_h(V) = 0.07\exp(-(V + 58)/20)$$

$$\beta_h(V) = 1/(\exp(-0.1(V + 28)) + 1)$$

c) OLM in CA1:

We modeled OLM neurons as described in (Wulff et al., 2009).

$$V_{Na} = 60[mV], V_K = -100.0[mV], V_L = -70.0[mV], V_A = -90.0[mV], V_h = -32.0[mV]$$

$$g_{Na} = 40.0[mS/cm^2], g_K = 23.0[mS/cm^2], g_A = 16.0[mS/cm^2], g_h = 6.0[mS/cm^2], g_L = 0.05[mS/cm^2]$$

$$C = 1.3, I_{cnst} = 0.2$$

$$C\frac{dV_i}{dt} = g_{Na}m^3h(V_{Na} - V_i) + g_K n^4(V_K - V_i) + g_A ab(V_A - V_i) + g_h r(V_h - V_i) + g_L(V_L - V_i) + I_i + I_{cnst}$$

$$\frac{dx}{dt} = \frac{x_\infty(V) - x}{\tau_x(V)}, \quad \text{(Eq.2)}$$

where $x = m$, h, n, a, b and r. The channel variables are determined by

$$x_\infty(V) = \frac{\alpha_x(V)}{\alpha_x(V) + \beta_x(V)},$$

$$\tau_x(V) = \frac{1}{\alpha_x(V) + \beta_x(V)}.$$

for m, h and n with

$$\alpha_m(V) = -\frac{0.1(V + 38)}{\exp\left(-\frac{v + 38}{10}\right) - 1}$$

$$\beta_m(V) = 4\exp(-\frac{V + 65}{18})$$

$$\alpha_h(V) = 0.07\exp(-\frac{V + 63}{20})$$

$$\beta_h(V) = 1/(\exp(-0.1(V + 33)) + 1)$$

$$\alpha_n(V) = \frac{0.018(V-25)}{1-\exp\left(-\frac{V-25}{25}\right)}$$

$$\beta_n(V) = \frac{0.0036(V-35)}{\exp\left(\frac{V-35}{12}\right)-1}$$

For $x = a$, b and r, variables in Eq.2 are determined by

$$a_\infty(V) = 1/(1+\exp\,(-(V+14)/16.6))$$

$$\tau_a(V) = 5$$

$$b_\infty(V) = 1/(1+\exp\,((V+71)/7.3))$$

$$\tau_b(V) = 1/(\frac{0.000009}{\exp\left(\frac{V-26}{18.5}\right)} + \frac{0.014}{0.2+\exp\left(-\frac{V+70}{11}\right)})$$

$$r_\infty(V) = 1/(1+\exp\,((V+84)/10.2))$$

$$\tau_r(V) = 1/(\exp(-14.59-0.086V)+\exp\,(-1.87+0.0701V))$$

d) Excitatory neurons in MECIII

We modeled excitatory neurons in MECIII based on an excitatory neuron model of MECII (Middleton et al., 2008), with some modifications of parameter values. These neurons have an AHP current in addition to the standard sodium, potassium and leak currents. The model is described as

C=1.0 [uF/cm^2],

$$V_{Na} = 50[mV], V_K = -90.0[mV], V_{AHP} = -100.0[mV], V_L = -65.0[mV]$$

$$g_{Na} = 100.0\left[\frac{mS}{cm^2}\right], g_K = 80.0\left[\frac{mS}{cm^2}\right], g_{AHP} = 0.3\left[\frac{mS}{cm^2}\right]$$

$$g_L = 0.5[mS/cm^2]$$

$$C\frac{dV_i}{dt} = g_{Na}m^3h(V_{Na}-V_i) + g_Kn^4(V_K-V_i) + g_{AHP}w(V_{AHP}-V_i) + g_L(V_L-V_i) + I_i$$

$$\frac{dx}{dt} = \alpha_x(V)(1-x) - \beta_x(V)x,$$

where $x = m$, n and h.

$$\alpha_m(V) = -0.32(V+54)/(\exp(-0.25*(V+54))-1)$$

$$\beta_m(V) = 0.28(V+27)/(\exp(0.2*(V+27))-1)$$

$$\alpha_n(V) = -0.032(V+52)/(\exp(-0.2*(V+52))-1)$$

$$\beta_n(V) = 0.5\exp\,(-0.025(V+57))$$

$$\alpha_h(V) = 0.128\exp\,(-(V+50)/18)$$

$$\beta_h(V) = 4.0/\exp\,(-0.2(V+27)+1).$$

The channel variable w is determined by

$$\frac{dw}{dt} = (w_\infty(V)-w)/\tau_w(V),$$

$$w_\infty(V) = \frac{1}{\exp(-0.1(V+41))+1},$$

$$\tau_\infty(V) = \frac{500}{3.3\exp\big(0.05(V+41)\big) + \exp\big(-0.05(V+41)\big)}.$$

e) Excitatory neurons in MECV

excitatory neurons in MECV are modeled based on (Egorov et al., 2002; Fransén et al., 2006) with simplification of conductance of nonspecific calcium-sensitive cationic, g_{CAN} (see Disinhibitory system in STAR Methods). Ca flux is regulated through CaL channel.

$$V_{Na} = 50[mV], V_K = -100[mV], V_{CAN} = -20[mV], V_{Ca} = 140[mV], V_L = -65[mV]$$

$$g_{Na} = 100.0\left[\frac{mS}{cm^2}\right], g_K = 80.0\left[\frac{mS}{cm^2}\right], g_{AHP} = 0.05, g_{K,C} = 195\left[\frac{mS}{cm^2}\right], g_{K,C} = 195\left[\frac{mS}{cm^2}\right], g_M = 3.5, g_{CaL} = 0.15, g_{Na,p} = 0.2, g_{K,A} = 0.5, g_L = 0.5[mS/cm^2]$$

$C\frac{dV_i}{dt} = g_{Na}m^3h(V_{Na} - V_i) + g_Kn^4(V_K - V_i) + g_{AHP}w(V_{AHP} - V_i) + g_Ms_M(V_K - V_i) + g_{Na,p}\,s_{Na,p}\,h_{Na,p}\,(V_{Na} - V_i) + g_{K,A}s_{K,A}h_{K,A}(V_K - V_i) + g_{CAN}(t)s_{CAN}(V_{CAN} - V_i) + g_{K,C}\,s_{KC}(V_K - V_i) + + g_{CaL}s_{CaL}(V_{Ca} - V_i) + I_i$ (Eq.3)

In addition to voltage dynamics, concentration of Ca^{2+}, $[Ca^{2+}]$, in a neuron is modeled according to:

$$\frac{d[Ca^{2+}]}{dt} = \kappa I_{CaL} - [Ca^{2+}]/\tau_{Ca}$$

Here, $\kappa = 0.5181937[Fd^{-1}]$ and $\tau_{Ca} = 250[ms]$.

The standard current of sodium and potassium in Eq.3 are exactly same as in excitatory neurons in MECIII. AHP, KA, KC, M, Na_p and CaL currents follow the standard activation-inactivation forms:

$$\frac{dx}{dt} = \alpha_x(V)(1-x) - \beta_x(V)x$$

$$x = w(=AHP), s_M(=M), s_{K,A}, h_{K,A}, s_{K,C}\,(=KC), s_{CaL}(=CaL).$$

α and β of each current are according to the following equations.:

$$\alpha_{AHP}(V) = \begin{cases} \min(2.4([Ca^{2+}] - 15), 15) & \text{for } [Ca^{2+}] > 15 \\ 0.2[Ca^{2+}] & \text{otherwise} \end{cases}$$

$$\beta_{AHP}(V) = 1$$

$$\alpha_{CaL}(C) = \frac{1.6}{1 + \exp\big(-0.072(V-65)\big)}$$

$$\beta_{CaL}(V) = \frac{0.02(V-51.1)}{\exp\big(0.2(V-51.1)\big) - 1}$$

$$\alpha_{KC}(V) = \begin{cases} \dfrac{\exp(0.053782V - 0.66835)}{18.975} & \text{for } V < 50 \\ 2\exp\left(\dfrac{6.5 - V}{27}\right) & \text{otherwise} \end{cases}$$

$$\beta_{KC}(V) = \begin{cases} 2\exp\left(\frac{6.5 - V}{27}\right) - \alpha_{KC} & \text{for } V < 50 \\ 0 & \text{otherwise} \end{cases}$$

$$\alpha_{s_{KA}}(V) = \frac{0.02(V - 13.1)}{1 - \exp\big(0.1(13.1 - V)\big)}$$

$$\beta_{s_{KA}}(V) = \frac{0.175(V - 40.1)}{\exp\big(0.1(V - 40.1)\big) - 1}$$

$$\alpha_{h_{KA}}(V) = 0.0016\exp\,(-(V + 13)/18)$$

$$\beta_{h_{KA}}(V) = 0.05/(1 + 0.2\exp(10.1 - V))$$

Variables for M, Na_p and CAN channels follow the form:

$$\frac{dx}{dt} = \frac{x_\infty(V) - x}{\tau_x(V)},$$

where $x = s_{Na,p}, h_{Na\cdot p}, s_M(= M), s_{CAN}(= CAN)$. x_∞ and τ_x for each variables are according to

$$s_{M,\infty}(V) = 1/(1 + \exp\,(-V + 35)/5)$$

$$\tau_M(V) = \frac{1000}{3.3\exp((V + 35)/40) + \exp\,(-(V + 35)/20)}$$

$$s_{Na,p\infty}\,(V) = 1/(1 + \exp\left(-\frac{V + 48.7}{4.4}\right))$$

$$\tau_{s_{Na_p}}(V) = \frac{1}{\left(\frac{0.091(V + 38)}{1 - \exp\left(\frac{V + 38}{5}\right)} - \frac{0.062(V + 38)}{1 - \exp\left(\frac{V + 38}{5}\right)}\right)}$$

$$h_{Na,p\infty}\,(V) = \frac{1}{1 + \exp\left(-\frac{V + 48.8}{9.98}\right)}$$

$$\tau_{h_{Na,p}}\,(V) = \frac{1}{-\frac{0.00000288(V - 49.1)}{1 - \exp\left(-\frac{V - 49.1}{4.63}\right)} + -\frac{0.00000694(V + 44.7)}{1 - \exp\left(-\frac{V + 44.7}{2.63}\right)}}$$

$$s_{CAN,\infty}(V) = 48 \times \frac{10^2[Ca^{2+}]^2}{48 \times 10^2[Ca^{2+}]^2 + 0.03}$$

$$\tau_{s_{CAN}}(V) = 1/(48 \times 10^2[Ca^{2+}]^2).$$

Synaptic Inputs

Synaptic input I_i to neuron i includes excitatory I_i^E and inhibitory I_i^I currents. Only in CA1 neurons, OLM currents, which are from OLM neurons, are modeled as another type of inhibitory currents based on (Wulff et al., 2009).

$$I_i(t) = I_i^E + I_i^I = g_i^E(V_E - V) + g_i^I(V_I - V) + g_i^{OLM}(V_i - V)$$

$$g_i^{E,I,OLM}(t) = \Sigma_k \int_0^t G_{ik}\Sigma_s \alpha^{E,I,OLM}(t' - t_k^s - d_{ik})dt' \quad \text{(Eq.4)},$$

where k is index of pre-synaptic neuron. For the excitatory current, k corresponds to index of excitatory neurons in all cortical areas and excitatory noise neurons projecting to post-synaptic neuron *i*. For the inhibitory currents, *k* corresponds to index of inhibitory neurons (PV, OLM, VIP, GABA) in all cortical areas and inhibitory noise neurons projecting to post-synaptic neuron *i* . Connections *G* among these neurons are described in Circuit model in STAR Methods. *s* is index of spikes in *k* neuron. d_{ik} is transduction time lag. When neurons *i* and *k* are within a same area, *d* is chosen randomly from (0,2) ms, while *d* is chosen from (10,15) ms for neurons in different areas. Double exponential functions, α, are described as:

$$\alpha^{E,I,OLM}(t) = (e^{-\frac{t}{\tau^r_{E,I,OLM}}} - e^{-\frac{t}{\tau^d_{E,I,OLM}}})/(\tau^r_{E,I,OLM} - \tau^d_{E,I,OLM}) \text{ (Eq.5)}$$

Rise time constant t^r is 0.05,0.07 and 2.0 ms for E, I, and OLM, respectively, while decay time constant t^d is 5.3, 9.1 and 22.0 ms for E, I, and OLM, respectively.

Circuit structure

Our model has three cortical areas (Figure1A) and external oscillating neurons in MECII, CA3 and MS. excitatory neurons in each cortical area are divided into two or four subgroups (Table1). CA1 has four groups denoted as Left (L), Right (R), Center (C) and Home (H). MECIII and MECV have two groups denoted as L and R.

Table1: number of neurons in each are

	CA1	ECIII	ECV	CA3
E	120x4	120x2	200x2	120x4
PV	240	160	120	
OLM	240			

In addition, a model has 240 VIP neurons in CA1, 120 excitatory neurons in MECII and 360 GABAergic neurons in MS. The GABAergic neurons are divided into three groups projecting to different types of neuron each of which has 120 neurons; groups to OLM, to PV in CA1 and to PV in MECV.

Structure of a circuit is given by a matrix *G* in Eq. 4, which represents efficacy of synaptic connections. Connection between presynaptic neuron *j* and postsynaptic neuron *I*, G_{ij} is determined by

$$G_{ij} = \begin{cases} G_{XY}^{AB} / \rho_{XY}^{AB} N_Y^B & \text{with probability } \rho_{XY}^{AB} \\ 0 & \text{otherwise} \end{cases} \quad \text{(Eq.6)},$$

where X and Y are neuron types that *i* and *j* neurons belong to, respectively. A and B refer subgroups (L,R,C,and H) that *i* and *j* neurons belong to, respectively. Because only excitatory neurons in each area are divided as the subgroups, A and B are neglected for other types of neurons. N_Y is the number of type *Y* neurons. If the type Y neurons are divided into the subgroup, $N^B{}_Y$ indicates the number of type Y neurons in subgroup B. *G* and ρ for each connection are as follows:

i) Connection from noise neurons

Connections *G* from noise neurons to the neurons in cortical areas are shown in Table2. A postsynaptic neuron receives inputs from 40 excitatory and 40 inhibitory neurons ($\rho_{XY} = 1, N_{XY} = 40$).

Table2 Connection G_{XY} from noise neurons to each type of neurons.

Post-synaptic X / Pre-synaptic Y	CA1			ECIII		ECV	
	E	PV	OLM	E	PV	E	PV
Excitatory noise neurons	.32	.8	3.2	.8	.2	.2	.4
Inhibitory noise neurons	.6	.2	.4	.6	.8	.2	.6

ii) Connection from excitatory neurons in MECII, MS and CA3

a) connection from excitatory neurons in MECII to PV in MECIII

$$G_{XY} = 0.4$$
$$\rho_{XY} = 1$$

b) from GABAergic neurons in MS

to PV in MECV

$$G_{XY} = 0.1$$

to PV in CA1

$$G_{XY} = 3.7$$

to OLM in CA1

$$G_{XY} = 3.7$$

For all connections,

$$\rho_{XY} = 1$$

c) from CA3 to E in CA1

for $A \neq B$

$$G_{XY}^{AB} = 0, \rho_{XY}^{AB} = 0$$

For $A = B$

$$G_{XY}^{AB} = 2.0\xi, \rho_{XY}^{AB} = 0.3$$

here, ξ is chosen randomly from (0,1).

d) from CA3 to PV in CA1

$$G_{XY} = 0.1 \ \ \rho_{XY} = 0.5.$$

e) from VIP to PV and OLM in CA1

Efficacy of these connections are modified by [ACh] (Tremblay et al., 2016) as follows:

For X=PV,

$$G_{XY} = 0.012[Ach], \rho_{XY} = 1$$

For X=OLM,

$$G_{XY} = 0.02[Ach], \ \rho_{XY} = 1$$

f) Connections between E neurons within the same cortical areas

For $A \neq B$

$$G_{XY}^{AB} = 0.01, \rho = 0.025 \ (\text{in MECIII})$$
$$G_{XY}^{AB} = 0, \rho = 0 \ (\text{in MECV})$$

For $A = B$

$$G_{XY}^{AB} = 14.4, \rho = 0.15 \ (\text{in MECIII})$$
$$G_{XY}^{AB} = 0.216, \rho = 0.03 \ (\text{in MECV})$$

There is no connections between excitatory neurons in CA1 in our model.

g) Connection between neurons within the same cortical areas (except E-E connections)

There is no connections between OLMs(Wulff et al., 2009). Connections from OLM to E neurons in CA1 are described in h), since OLM is observed to be attached on proximal dendrite of excitatory neurons in CA1 and regulate inputs from MECIII.

Other connections within cortical areas are shown in Table 3.

Table 3: connection parameters in CA1, MECIII, MECV

	CA1					
(X,Y)	E,PV	PV,E	PV,PV	PV,OLM	OLM,E	OLM,PV
G_{XY}	2.2	0.2	0.3	0.5	0.5	0.2
ρ_{XY}	0.5	0.5	0.5	0.5	0.3	0.5

MECIII			MECV		
E,PV	PV,E	PV,PV	E,PV	PV,E	PV,PV

2.5	0.5	0.01	0.2	0.3	0.01
0.5	0.3	0.3	0.5	0.3	0.3

h) connections from neurons in CA1 to those in MECV

For X=excitatory neurons in MECV, Y=excitatory neurons in CA1,

$$G_{XY}^{AB} = \begin{cases} 0.27 & \text{for } B \in \{H, C\} \\ 0.36 \text{ for } (A,B) \in \{(L,L),(R,R)\} \\ 0.00125 & \text{otherwise} \end{cases}, \rho_{XY}^{AB} = \begin{cases} 0.075 & \text{for } B \in \{H, C\} \\ 0.075 \text{ for } (A,B) \in \{(L,L),(R,R)\} \\ 0.0125 & \text{otherwise} \end{cases}$$

For X=PV neurons in MECV, Y=excitatory neurons in CA1,

$$G_{XY} = 0.01, \qquad \rho_{XY} = 0.3$$

i) connections from neurons in MECV to those in MECIII

For X= excitatory neurons in MECIII, Y=excitatory neurons in MECV,

$$G_{XY}^{AB} = \begin{cases} 0.01 \text{ for } A \neq B \\ 1.44 \text{ otherwise} \end{cases}, \rho_{XY}^{AB} = \begin{cases} 0.0125 \text{ for } A \neq B \\ 0.075 \text{ otherwise} \end{cases}$$

j) connections from neurons in MECIII to those in CA1

For X=excitatory neurons in CA1, Y=excitatory neurons in MECIII,

$$G_{XY}^{AB} = \begin{cases} 0.003 for A \neq B \\ 0.216 otherwise \end{cases}, \rho_{XY}^{AB} = \begin{cases} 0.01 for A \neq B \\ 0.06 otherwise \end{cases}$$

In addition, effect of OLM is implemented for modulating inputs from MECIII as follows:

Up to 5 ms after a spike from OLM to a E neurons in CA1, efficacy of connections from E neurons in MECIII to this E neurons in CA1 is reduced with multiplication by 0.1.

Nonlinear interaction of excitatory neurons in CA1 with input from MECIII and CA3

E neurons integrate spikes from CA3 and MECIII (Bittner et al., 2015). We introduced this effect in our model. A prolonged EPSC I_{prol} is supposed to be generated, when the following conditions are satisfied:

- A excitatory neuron in CA1 receives a burst (three spikes within 15ms) from MECIII and it does not receive any inhibitory input from OLM within 15ms at time t_1.
- This excitatory CA1 receives a burst (three spikes within 10ms) from CA3 within 20ms from t_1 (denoted t_2).
- Previous prolonged EPSC is 100ms earlier than t_2.

If these conditions are satisfied, a prolonged (100ms) EPSC in E neuron in CA1 is generated according to:

$$\alpha_{prol}(t) = \begin{cases} \frac{t}{5} \text{ for } 0 < t < 5[ms] \\ 1 - \frac{t-5}{60} \text{ for } 5 < t < 35 \\ 0.5 \exp\left(-\frac{t-35}{30}\right) \text{ for } 35 < t < 100 \\ 0 \quad \text{otherwise} \end{cases}$$

$$I_{prol}(t) = 0.01\alpha_{prol}(t)$$

Disinhibitory system and modulated conductance of nonspecific calcium-sensitive cationic (CAN) current through ACh.

We assume concentration of ACh represents cognitive states and changes dependent of current locations:

$$[\text{ACh}] = \begin{cases} 0.2 \text{ for } t < 1[\text{s}] \text{ (a rat on sample-C)} \\ 1 - 0.8exp\left(-\frac{t-T_{LS}}{200}\right) \text{ for } 1[\text{s}] \le t < 3[\text{s}] \text{ (a rat on sample-L)} \\ 0.8 - 0.2exp\left(-\frac{t-T_{H}}{200}\right) \text{ for } 3[\text{s}] \le t < 4.5[\text{s}] \text{ (a rat on sample-L)} \\ 1.1 - 0.3exp\left(-\frac{t-T_{CT}}{200}\right) \text{ for } 4.5[\text{s}] \le t \text{ (a rat on test-C)} \end{cases}$$

[ACh] modifies neural behavior in a circuit in two pathways. Efficacy of connections from VIP is modified with [ACh] (Circuit structure in STAR Methods) as well as conductance of I_{CAN}. Maximum conductance g_{CAN} is dependent on history of [Ca2+] and [ACh] (Fransén et al., 2006) as follows:

$$g_{CAN}(t) = 0.02[Ach]r_{high}(t)$$

$$r_{high}(t+\Delta t) = \begin{cases} r_{high}(t) + 1.5\Delta t \text{ for } [Ca^{2+}] > 0.004 \\ r_{high}(t) - 0.2\Delta t \text{ for } [Ca^{2+}] < 0.0003 \\ r_{high}(t) \quad \text{otherwise} \end{cases}$$

We also set upper and lower bounds for r_{high} at 2.5 and 0.3, respectively.

An additional decoder

To examine how high gamma coherence between MECIII and CA1 observed in (Yamamoto et al., 2014) is utilized for detection of previous memories, we applied stimuli with high gamma oscillation to these areas and implemented an additional circuit as a decoder. The decoder circuit composes 100 excitatory (exc) and 100 inhibitory (inh) neurons (Figure 7A) which receive synaptic inputs from excitatory neurons in MECIII and CA1. For the high gamma stimuli, we applied coherent current input $I_{\text{high }\gamma}$ to excitatory neurons in CA1 and ECIII with f=80 Hz as follows:

$$r_t = \sin(2\pi f t/1000), \text{ here } t\text{=}t[\text{ms}],$$

$$I_{\text{high }\gamma} = \begin{cases} 0.02 m r_t \text{ for } m r_t > 0 \\ I_0 r_t \text{ for } r_t \le 0 \end{cases},$$

$I_0 = 0.18$ for CA1 neurons, 0.216 for ECIII neurons.

Excitatory neurons are modeled as a normal HH neuron model:

$$C = 1.0[\mu F/cm^2]$$

$$V_{Na} = 50[mV], V_K = -90.0[mV], V_L = -65.0[mV]$$

$$g_{Na} = 100.0[mS/cm^2], g_K = 80.0[mS/cm^2], g_L = 0.5[mS/cm^2]$$

$$C\frac{dV_i}{dt} = g_{Na} m^3 h (V_{Na} - V_i) + g_K n^4 (V_K - V_i) + g_L (V_L - V_i) + I_i + 0.1$$

$$\frac{dx}{dt} = \alpha_x(V)(1-x) - \beta_x(V)x,$$

where x=m,n,and h.

$$\alpha_m(V) = -0.32(V+54)/(\exp(-0.25 * (V+54)) - 1)$$

$$\beta_m(V) = 0.28(V+27)/(\exp(0.2 * (V+27)) - 1)$$

$$\alpha_n(V) = -0.032(V+52)/(\exp(-0.2 * (V+52)) - 1)$$

$$\beta_n(V) = 0.5\exp(-0.025(V+57))$$

$$\alpha_h(V) = 0.128\exp(-(V+50)/18)$$

$$\beta_h(V) = 4.0/\exp(-0.2(V+27)+1).$$

Inhibitory neurons are modeled same as PV neurons in CA1, MECIII and MECV. Neurons in the decoder receive noisy excitatory and inhibitory synaptic inputs same as those in the main circuit (inputs from noise neurons in Synaptic structure). Excitatory and inhibitory neurons spike with 35[Hz]. Connection strength from 40 excitatory noise neurons to excitatory and inhibitory ones in the decoder, $G_{EE}, G_{IE} = 0.005, 0.05$, while those from 40 inhibitory noisy neurons to excitatory and inhibitory ones in the decoder, $G_{EI}, G_{II} = 0.02, 0.0015$. For alpha function in Eq.5 for both of the excitatory and inhibitory neurons in the decoder, we set τ_{dcy} =4 ms and other parameters are same as the main circuit.

In the decoder circuit, 100 excitatory neurons are divided into two sub groups, L (50 neurons) and R (50 neurons), as well as 100 inhibitory neurons. Synaptic inputs from these neuron and excitatory neurons in CA1 and MECIII are modeled as Eq.4. Circuit structure of the decoder is set according to Table 4. We also set time-lag d through synaptic inputs; d from MECIII and CA1 to the excitatory neurons is chosen randomly from (35,50) and (10,15) ms, respectively. d from those to the inhibitory neurons is chosen randomly from (22.5,27.5) and (10,15) ms, respectively.

Table 4: circuit structure of the decoder

pre / post	E	I	E in CA1	E in MECIII
E	0 0	2.5 0.8	0.4 0.1	0.02 0.1
I	0 0	0.05 0.6	0.45 0.4	0.3 0.2

For each cell, upper and lower values are $G_{post,pre}$ and $\rho_{post,pre}$ in Eq.6, respectively.

We implemented nonlinear amplifications of inputs from MECIII and CA1 as similar to that in the excitatory neurons in CA1. To be specific, when both inputs arrive to the neuron in the decoder within 1 ms, input currents are amplified by 4.5-fold and 2.0-fold in excitatory and inhibitory neurons, respectively.

Experimental data in rats

Spiking activities and LFP data in CA1 are obtained from previously published data in (Yamamoto et al., 2014) for Figures 5B and 6C and that in (Mizuseki et al., 2013) for Figures 5D and 5E. Experiments were approved by the Institutional Animal Care and Use Committee of Rutgers University. All procedures for animal care and use were performed in accordance with the National Institutes of Health *Guide for the Care and Use of Laboratory Animals*. Detailed conditions on data recording are described in these papers.

LFP activities were band-pass filtered (6-12Hz) as theta wave and instantaneous phase of the filtered theta wave were derived from Hilbert transform. For spiking activities, we dropped a part of spikes to analyzed as follows:

Spiking activities in (Yamamoto et al., 2014) were recorded with the silicon linear probes and were analyzed as multi-unit activities. In this paper, however, we roughly distinguish putative excitatory neurons from inhibitory ones in order to show clear theta preference. According to (Mizuseki et al., 2009), we sorted spikes by trough to peak latency. Due to short length of single spike profile in the data, we cannot identify baseline before spike and consequently cannot compute peak amplitude asymmetry. We assigned spikes with the latency larger than 0.5ms to putative excitatory neurons. For Figure 5B, we have the sorted spikes in three out of five rats because spikes of the rest two rats do not show clear theta preference due to small number of spikes.

For spiking activities in (Mizuseki et al., 2013), we used sessions "ec014.12","ec014.16","ec014.17","ec014.27","ec014.28","ec013.44","ec013.46","ec016.30". Because phase shift in the side arm was observed only in deeper neurons in

(Fernández-Ruiz et al., 2017), we only used spikes of deeper neurons according to (Mizuseki et al., 2011).

Figure 1

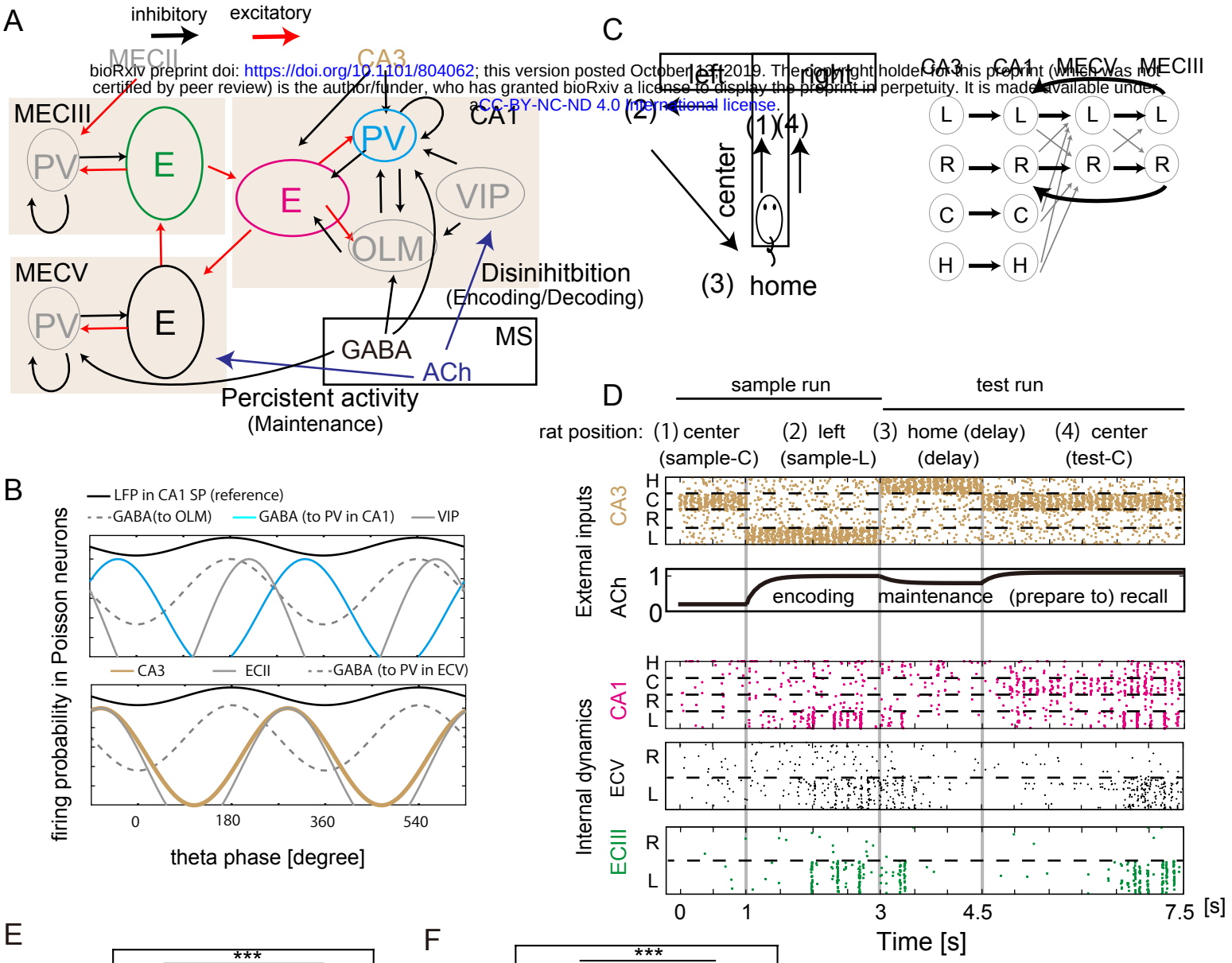

Figure 2

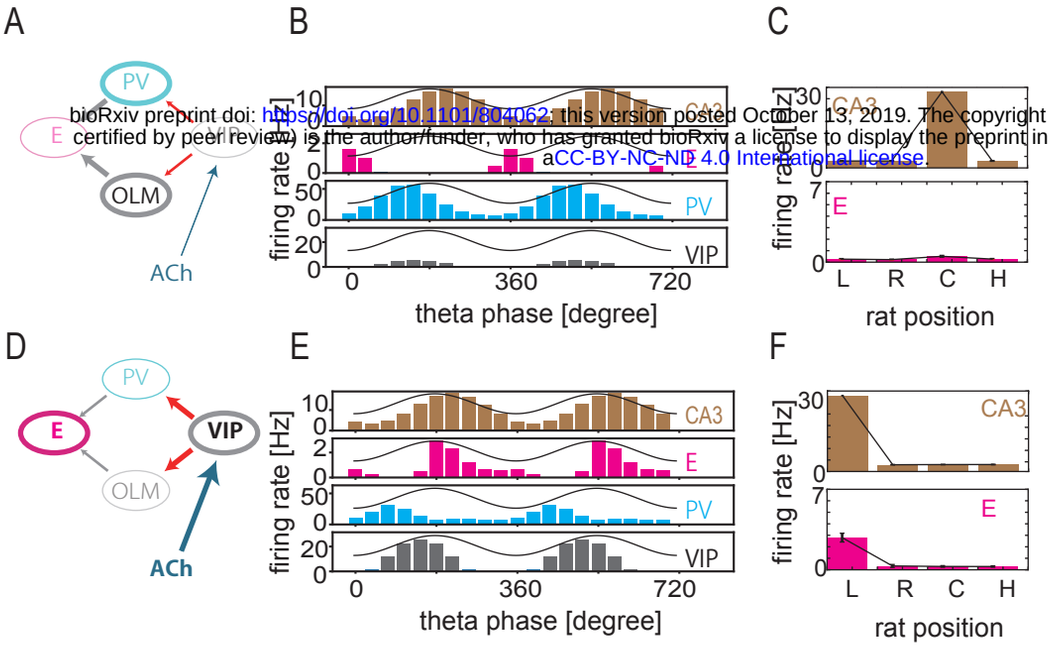

Figure 3

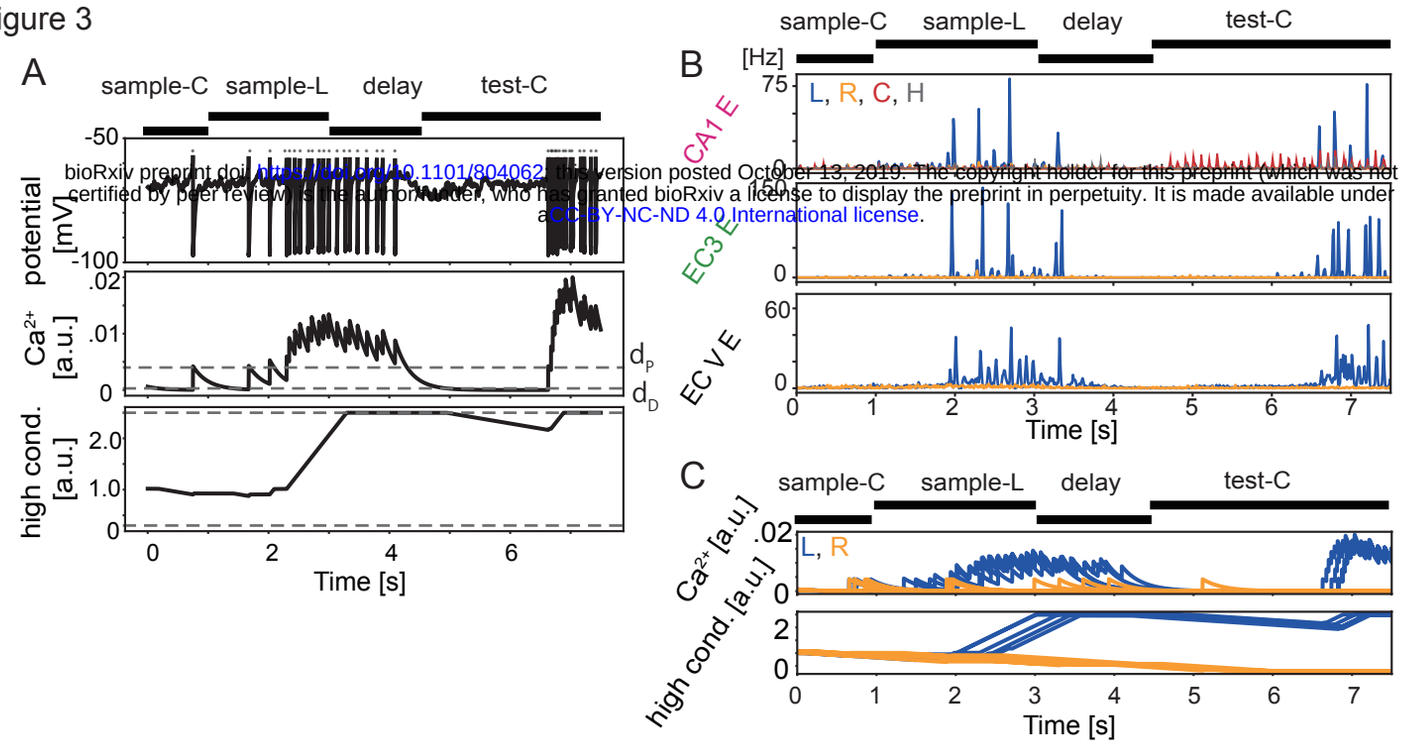

Figure 4

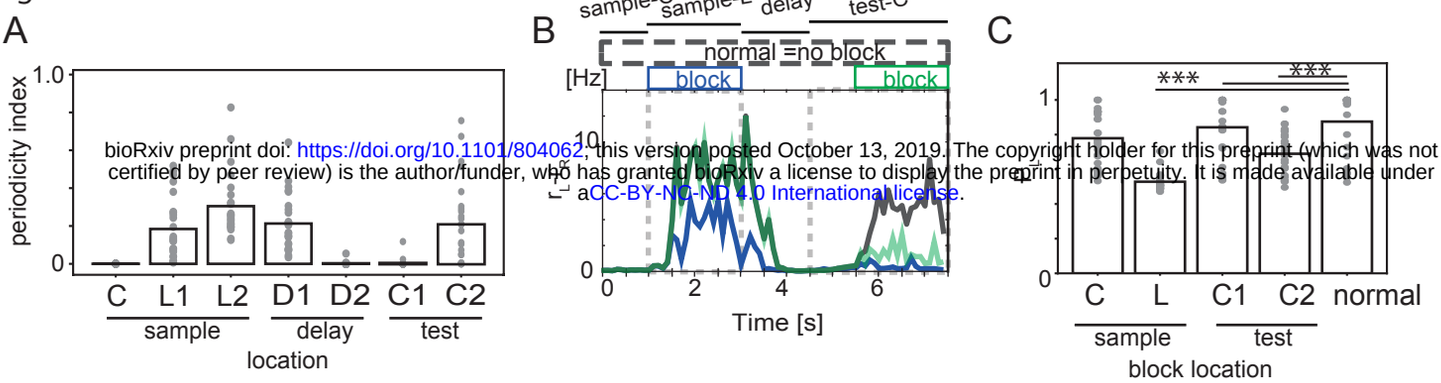

Figure 5

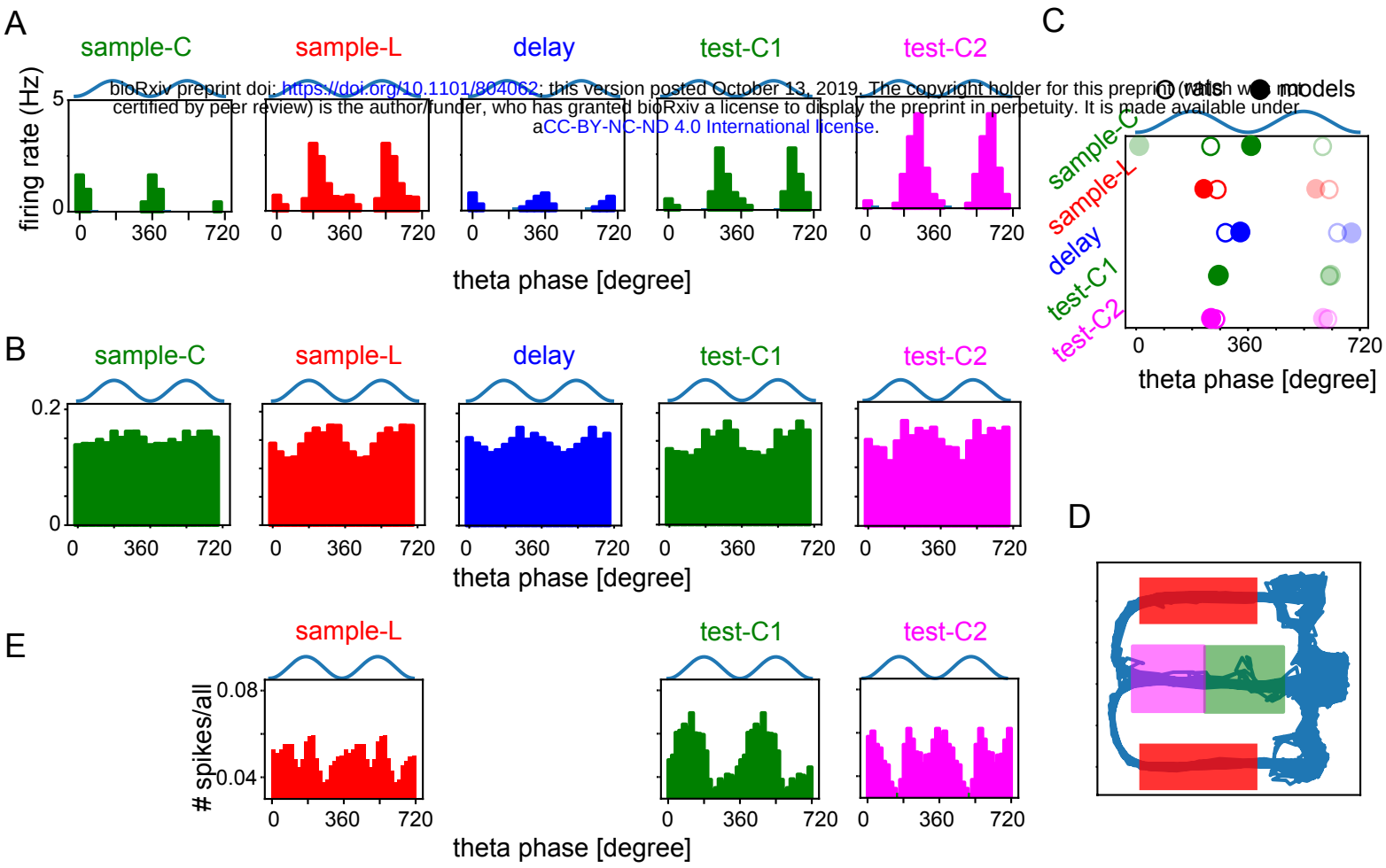

Figure 6

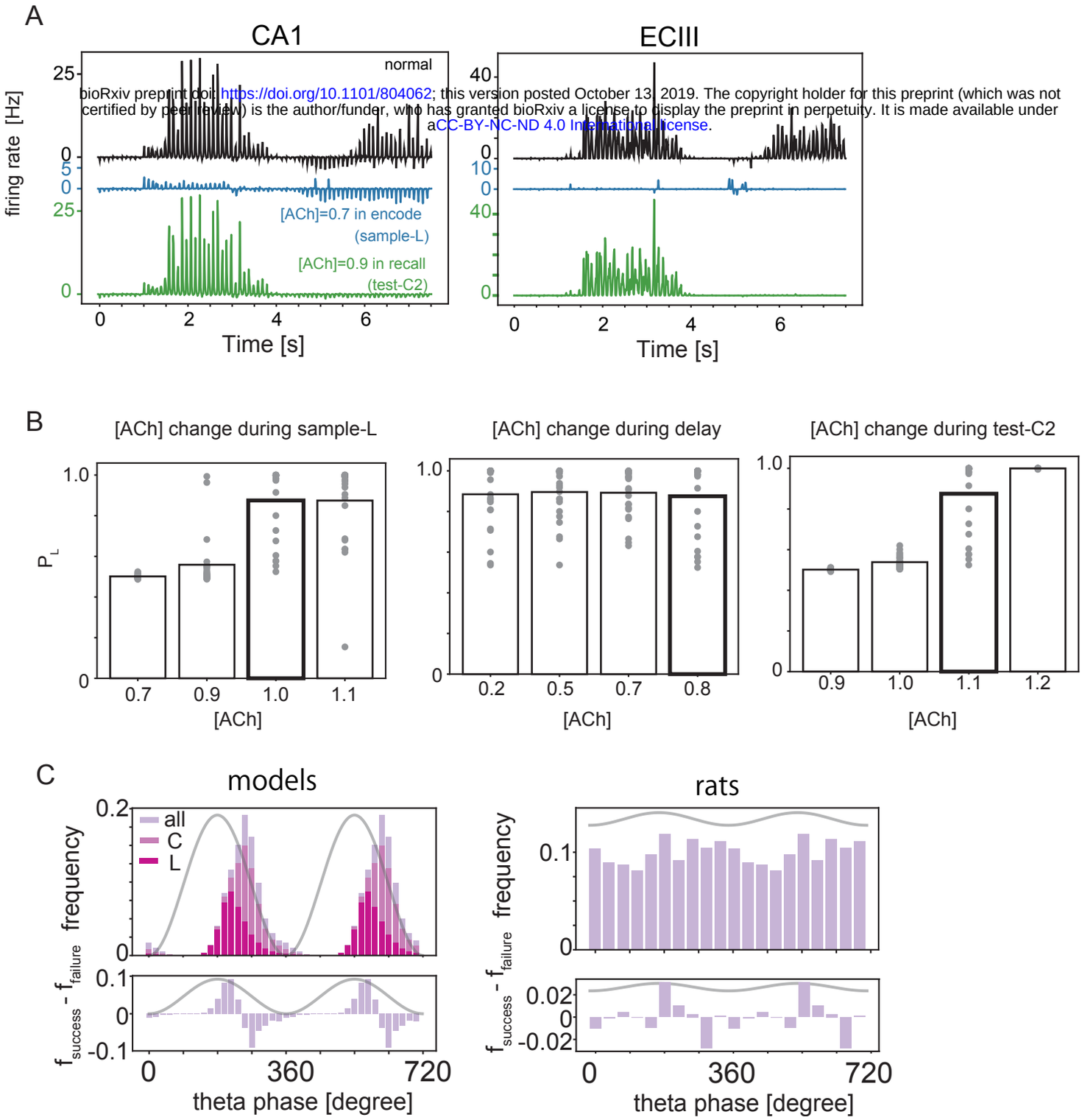

Figure 7